PROGRESS REPORT OF THE ASACUSA AD-3 COLLABORATION

Progress in 2021 and plans for 2022

ASACUSA collaboration

C. Amsler[a], D. Barna[b], H. Breuker[c], M. Bumbar[a], S. Chesnevskaya[a], G. Costantini[d], R. Ferragut[e], M. Giammarchi[f], A. Gligorova[a], G. Gosta[d], H. Higaki[g], M. Hori[h,i*], E. D. Hunter[a], Y. Kanai[j], C. Killian[a], V. Kletzl[a], V. Kraxberger[a], N. Kuroda[k], A. Lanz[a], M. Leali[d], V. Mäckel[a,c], G. Maero[l], C. Malbrunot[m], V. Mascagna[d], Y. Matsuda[k], S. Migliorati[d], D. J. Murtagh[a], Y. Nagata[n], A. Nanda[a], L. Nowak[m], F. Parnefjord Gustafsson[a], E. Pasino[l], W. Pirkl[h], M. Romé[l], M. C. Simon[a], M. Tajima[j], V. Toso[e], U. Uggerhøj[o], S. Ulmer[c], L. Venturelli[d], A. Weiser[a], E. Widmann[a*], T. Wolz[m], Y. Yamazaki[c], J. Zmeskal[a]

[a]Stefan Meyer Institute, [b]Wigner Research Centre for Physics, [c]Ulmer Fundamental Symmetries Laboratory, RIKEN, [d]Dipartimento di Ingegneria dell'Informazione, Università degli Studi di Brescia and INFN Pavia, [e]Politechnico di Milano, [f]INFN Milano, [g]Graduate School of Advanced Sciences of Matter, Hiroshima University, [h]Max-Planck-Institut für Quantenoptik, [i]Fakultät für Physik, Ludwig-Maximilians-Universität München, [j]Nishina Center for Accelerator-Based Science, RIKEN, [k]Institute of Physics, the University of Tokyo, [l]Dipartimento di Fisica, Università degli Studi di Milano and INFN Milano, [m]Experimental Physics Department, CERN, [n]Department of Physics, Tokyo University of Science, [o]Department of Physics and Astronomy, Aarhus University
* Co-spokespersons

Executive summary

In 2021 the **antiprotonic helium** group constructed and commissioned the experimental setup that included a new 6 m-long electrostatic beamline that transported the 100 keV antiproton beam to a cryogenic helium gas target in which $\bar{p}\text{He}^+$ atoms were formed. Multiple differential pumping stages isolated the helium gas target from the ultrahigh vacuum in the other parts of the ELENA experimental beamlines. The target, profile monitors, antiproton annihilation detectors, and differential pumping systems were validated using the H^- and antiproton beams. The antiprotons were focused into the helium target and a satisfactory setting was tentatively found which will allow us to carry out two-photon laser spectroscopy of several $\bar{p}\text{He}^+$ resonances in 2022.

A major upcoming publication for ASACUSA involves the unexpected behaviour that was observed in the laser resonance spectra of $\bar{p}\text{He}^+$ atoms implanted in liquid, superfluid, and supercritical phase helium targets. Also in 2021 the Amsterdam-Paris-Dubna collaboration utilized the experimental data on HD^+ molecular ions and on antiprotonic helium to set better limits on the hypothetical fifth force that may arise between hadrons and antihadrons. Efforts were continued by these groups to improve the precision of the three-body QED calculations of $\bar{p}\text{He}^+$, primarily in contributions due to the spin-orbit couplings and the one-loop self energy correction of the orbital electron.

For the proper utilization of the cold ELENA beam in the experiments, the beam window of the cryogenic target which is used to decelerate the 100 keV antiprotons to keV energy scales was carefully optimized. Experimental and theoretical work in collaboration with researchers of Helsinki University on the nuclear stopping and scattering effects of keV antiprotons in various materials were carried out. These studies will help us produce $\bar{p}\text{He}^+$ atoms in a small volume that can be irradiated with the lasers.

ASACUSA has provided the parts of the 43 beam profile monitors of ELENA. We are almost finished with the electrodes of the last 5 beam profile monitors of the new BASE-STEP, PUMA, and ASACUSA-2 beamlines. We thank the CERN technical staff for the great efforts in this collaboration, which also enabled ELENA to start up in such a timely manner for the AD experiments.

In 2022, the collaboration intends to carry out high-precision studies of the intense two-photon resonances of $\bar{p}\text{He}^+$ using the new experimental apparatus. R&D of high-precision lasers, an induction decelerator of novel design, and discussions of utilizing the ultrastable optical reference signals provided by optical fibers from national metrological institutions will be continued.

2021 was a particularly difficult year for the **antihydrogen group**. The ongoing pandemic situation disrupted our ability to bring personnel to CERN, affected the ability of manufacturers to keep to schedules, and interfered with supply lines all of which caused substantial delays.

Despite these setbacks, we find ourselves in a very strong position going into 2022. Using a newly built drift tube accelerator to bring the ELENA beam to the same energy as the previously used RFQD beam (120 keV), we could re-use the existing foil detector serving both as a beam profile monitor and a final degrader to capture a similarly large number of antiprotons (~ 1 million) per ELENA shot. A new cold bore and electrode stack was built for the Cusp mixing trap. The last components arrived due to a (more than) 4 months delay only in the last two weeks of beam time, so no tests with antiprotons were possible. The trap has been installed in the area with electrodes 10 K cooler than previously possible. Our systematic studies of plasma properties have allowed

us to produce plasmas of millions of electrons cooled to 25 K with cyclotron cooling alone, 100 K colder than our previous best. These improvements will translate into a much higher production rate and lower temperature and larger ground-state fraction of produced antihydrogen in 2022. We expect this year to produce a strong enough antihydrogen beam to commence first interaction studies with microwaves.

Other parts of the experiment are being developed. Our new positron accumulator has been installed and successfully trapped particles beginning the process of fully integrating into our systems. The antihydrogen detector is being upgraded to significantly increase the readout rate. A new setup for annihilation studies with slowly extracted antiprotons is being designed, supported by a grant received in 2021, and will be installed in 2022 allowing a parasitic use of antiprotons.

In parallel to the work on antihydrogen production and detection, experiments with our hydrogen beams continued with the aim of finalizing the cavity and surrounding static magnetic field configuration for the first Rabi hyperfine spectroscopy with antihydrogen, developing a method to deexcite Rydberg antihydrogen created in the mixing, and using the available beam to perform tests of Lorentz invariance in the context of the Standard Model Extension (SME). The homogeneity of the static magnetic field was found to be small enough at low field, compensation coils will need to be developed for the stray fields in the antihydrogen experiment in 2022. First deexcitation results of Rydberg hydrogen, allowing to judge its feasibility and to plan its installation in the antihydrogen experiment, are envisioned by the end of 2022. Final results of the measurement of SME coefficients will become available in the next six months.

Contents

Part I

Antiprotonic Helium

1 Status of the physics

1.1 Introduction and summary of the 2021 theoretical progress

Antiprotonic helium ($\bar{p}\text{He}^+$) [1–24] which consists of a helium nucleus, an electron populating the 1s state, and an antiproton in a Rydberg state with principal and angular momentum quantum numbers of $n \approx \ell + 1 \approx 38$ constitutes the hadron-antihadron quantum bound system having the longest known lifetime that can be experimentally produced. The collaboration aims to carry out sub-Doppler two photon laser spectroscopy [17, 25] of atomic resonances which have not been detected yet but are predicted to have very small natural widths (≈ 0.3 MHz) using the ELENA [26,27] beam. If these transitions of weak intensity can be detected, the experimental precision may in principle be ultimately improved by two orders of magnitude compared to previous experiments using a beam of much larger emittance and energy spread provided by the radiofrequency quadrupole
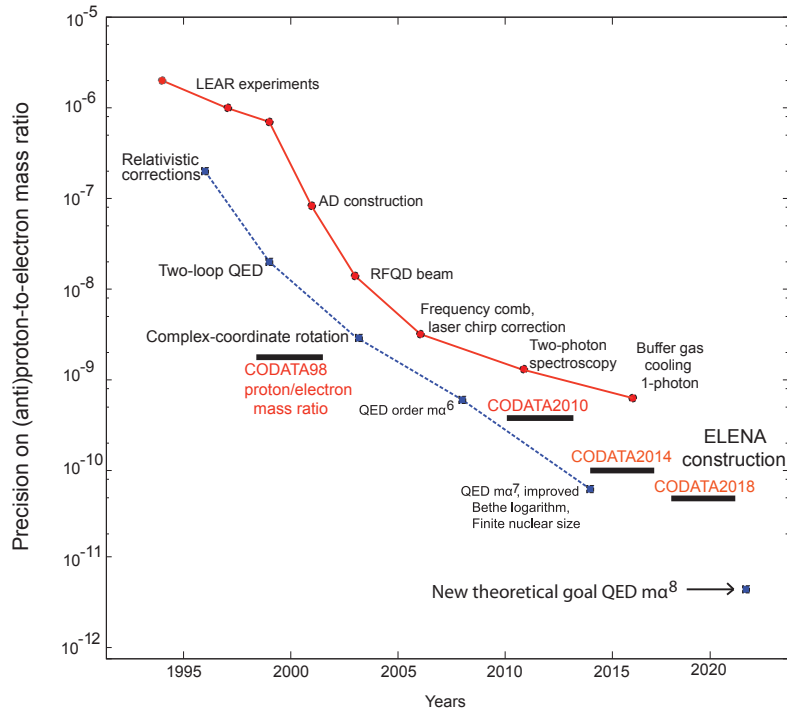
Figure 1 – Experimental precision on the antiproton-to-electron mass ratio determined by laser spectroscopy of $\bar{p}\text{He}^+$ over the years (solid red line), compared with the uncertainty of theoretical QED calculations (broken blue line). Efforts were continued in 2021 by the Paris and Dubna theoretical groups to improve the precision of the one-loop self-energy correction of the orbital electron in all orders of $(Z\alpha)^2$ and the spin-orbit parts of the state energies. The $\bar{p}\text{He}^+$ transition frequencies may reach $\sim 6 \times 10^{-12}$ within a few years. This corresponds to a factor > 400 higher precision compared to the best published results of ASACUSA in 2016. The relative precision of the latest Committee on Data for Science and Technology (CODATA) 2018 recommended value of the proton-to-electron mass ratio compiled in 2019 is shown.

decelerator (RFQD) [17, 20, 28, 29]; this would require many years of iterative work in terms of developing new metrological techniques and eliminating systematic uncertainties. The goals of the experiment and the corresponding progress in 2021 include,

1. A test of three-body quantum electrodynamics (QED) calculations at $\approx 10^{-11}$ scale precision which may be compared with recent experiments on hydrogen deuteride molecular ions (HD$^+$) [30, 31]. These constitute among the most precise calculations carried out on bound-state systems. Theoretical efforts were continued in 2021 by Dubna and Paris researchers to improve the precision of both the $\bar{p}$He$^+$ and HD$^+$ [11, 32, 33] calculations with a tentative goal of achieving a relative precision of $\approx 6 \times 10^{-12}$ within a few years. Some of the intermediate theoretical results may soon be published.

2. A determination of the antiproton-to-electron mass ratio to 10^{-11}-scale precision [17, 20] which would improve the current value published by ASACUSA of $M_{\bar{p}}/m_e = 1836.1526734(15)$. Our value may then be compared with the proton-to-electron ratio determined by spectroscopy of HD$^+$. In 2020, the Düsseldorf-based collaboration [30] published a value,

$$M_p/m_e = 1836.152673449(24)_{\text{exp}}(25)_{\text{theor}}(13)_{\text{CODATA2018, Fink-Myers}}. \tag{1}$$

In the same year the Amsterdam-Paris based experiment determined the ratio based on a different set of HD$^+$ transitions [31],

$$M_p/m_e = 1836.152673406(38). \tag{2}$$

A series of experiments using magnetic Penning traps yielded values of M_p/m_e with similar precision [34, 35]. These multiple determinations of the (anti)proton-to-electron mass ratio using various atoms and molecules are complementary, since each experiment relies on different combinations of the masses and charge radii of the constituent electron, (anti)proton, deuteron, and ^{3}He and ^{4}He nuclei particles [36–42]. Compared to, e.g., the 1s-2s transition of atomic hydrogen, the $\bar{p}$He$^+$ transition frequencies studied by us are relatively insensitive to the uncertainties of the charge radii of the (anti)proton (size of contribution to the transition frequency < 1 MHz) and helium nucleus (4–7 MHz) since these Rydberg orbitals have very little overlap with the nucleus, and Coulomb repulsion reduces the spatial overlap between the antiproton and electron. Some of the masses and charge radii determinations of various experiments continue to differ from each other by many standard deviations, so efforts are underway in the community to reduce the systematic uncertainties. This would then afford highly sensitive methods to test bound-state QED calculations.

3. A consistency test of CPT symmetry in a bound hadron-antihadron system which is complementary to the studies carried out by the other AD experiments on antihydrogen (i.e., antilepton-antihadron system) and on a single antiproton [43–48].

4. Improved upper limits on fifth forces at angstrom-length scales [30, 49–54]. In 2021, the Amsterdam-Paris-Dubna collaboration published improved theoretical calculations of HD$^+$, $\bar{p}^3$He$^+$, and $\bar{p}^4$He$^+$ which led to better evaluations of the upper limits on such hypothetical forces that may arise between hadrons [55]. In 2018, constraints on velocity and spin-dependent, semi-leptonic forces between antihadrons and electrons due to axions or other undiscovered spin-0 or spin-1 bosons were obtained by a theoretical group using the $\bar{p}$He$^+$ data of ASACUSA [8, 56, 57]. Future improvements in the laser spectroscopic studies would lead to stronger constraints.

5. A major upcoming publication involves the unexpected behaviour that was observed in the laser resonance spectra of $\bar{p}\mathrm{He}^+$ implanted in liquid, superfluid, and supercritical phase helium targets. During 2021 the paper was very carefully prepared and it will soon be published [22].

In 2022, the collaboration intends to optimize the experimental conditions with the new ELENA beam and carry out high-precision studies of the intense two-photon resonances of $\bar{p}\mathrm{He}^+$ using the new beamline, experimental target, and laser systems. The collaboration continues R&D of high-precision lasers, and discussions of utilizing the ultrastable optical reference signals provided by optical fibers from national metrological institutions (NMI).

1.2 Progress in high-precision theoretical calculations of $\bar{p}\mathrm{He}^+$ and HD^+

In 2021 the theoretical collaboration of the Laboratoire Kastler Brossel Paris and JNIR Dubna published the latest calculation [33] of the rovibrational transition frequencies of HD^+ molecular ions. The researchers recalculated the one-loop and two-loop QED corrections of $m\alpha^7$ and $m\alpha^8$ orders using an adiabatic approximation. Higher-order corrections that arise from the polarizability of the deuteron were included. The improvements in the theoretical calculations when compared with the HD^+ experimental data allowed the proton-to-electron and deuteron-to-proton mass ratios to be determined with a precision of better than 2 parts in 10^{11}. Some of these theoretical methods can be applied to the $\bar{p}\mathrm{He}^+$ case.

Theoretical efforts are underway to calculate the spin-orbit contributions to the energies of $\bar{p}\mathrm{He}^+$ to higher precision, in continuation of work carried out in 2020 [32, 58]. Non-perturbative calculations of the one-loop self-energy correction of the orbital electron in all orders of $(Z\alpha)^2$ by using high-precision solutions of the two-center Dirac equations are also being studied.

1.3 New limits on exotic beyond-the-Standard Model forces

In 2021 the Amsterdam-Paris-Dubna collaboration used the agreement between the experimental and calculated resonance frequencies of three HD^+ transitions and four $\bar{p}^3\mathrm{He}^+$ and $\bar{p}^4\mathrm{He}^+$ transitions measured by ASACUSA to set a combined upper limit to the hypothetical scalar hadron-hadron interactions [55]. This is phenomenologically modelled in the form of a Yukawa-type "fifth force" potential,

$$V_{\alpha_5,\lambda}(r) = \hbar c \alpha_5 A_1 A_2 \frac{e^{-r/\lambda}}{r}. \tag{3}$$

Here r denotes the separation between the two nuclei (or between the antiproton and helium nucleus in the case of $\bar{p}\mathrm{He}^+$), α_5 the coupling constant of the so-called "fifth force", and λ the range of the interaction mediated by a hypothetical field of mass m_5. Fig. 2 (a) shows the new derived limits on the coupling α_5/α between 10^{-7} and 10^{-11} as a function of the length scale λ. The Düsseldorf-Dubna collaboration [30] in 2020 parameterized the force in the same form,

$$V_5(R) = \beta N_1 N_2 \frac{e^{-R/\lambda}}{R}, \tag{4}$$

and obtained the corresponding plot shown in Fig. 2 (b). The sensitivity of our $\bar{p}\mathrm{He}^+$ experiments to these force(s) becomes greater for small interparticle distances $\lambda < 0.2\text{Å}$ because of the small diameter of the $\bar{p}\mathrm{He}^+$ atom. A two orders of magnitude improvement in the precision of the ASACUSA experiments would significantly increase the exclusion zone at short length scales λ.
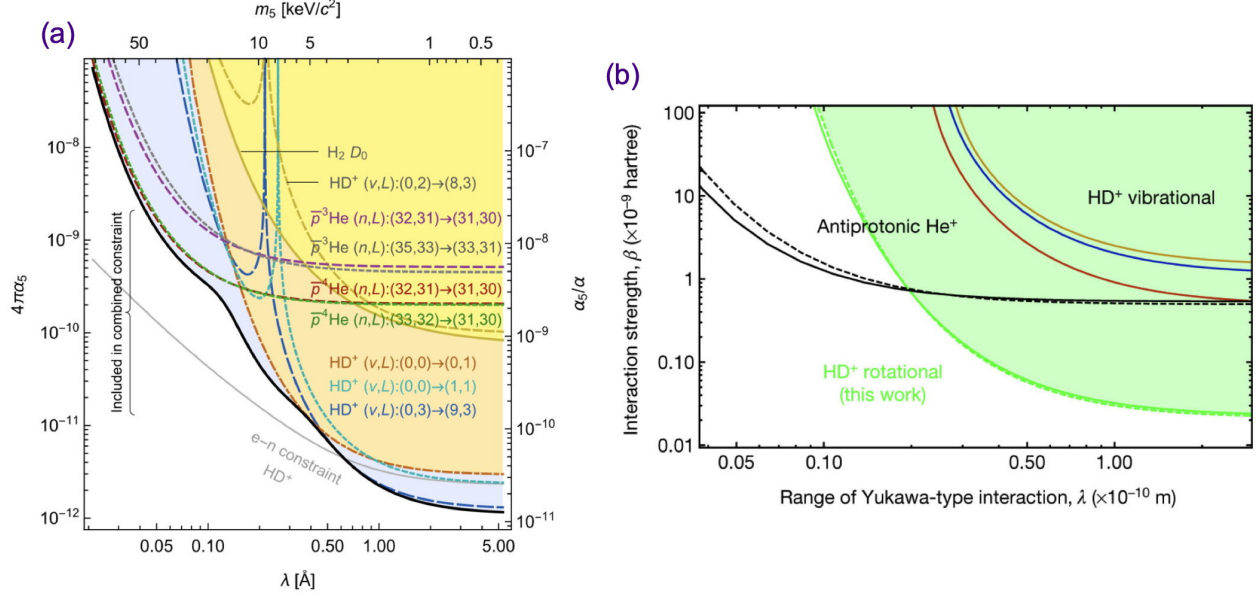
3

Figure 2 – (a): New exclusion plot of 90% confidence limit published in 2021 by the Amsterdam-Paris-Dubna collaboration for a scalar hadron-hadron interaction deduced by combining the experimental results for spectroscopy of HD^+, $\bar{p}^3He$, and $\bar{p}^4He$. From Ref. [55]. (b): Exclusion plot of 95% confidence limit for a Yukawa-type interaction between a proton and a deuteron deduced by spectroscopy of HD^+ carried out by the Düsseldorf collaboration in 2020 compared with the corresponding plot between an antiproton and ^4He nucleus determined by $\bar{p}He^+$. From Ref. [30].

2 Construction and commissioning of new experimental beamline and cryogenic target

2.1 New electrostatic beamline with differential pumping

In 2021 the collaboration constructed and commissioned a new 6 m long electrostatic beamline that transported the 100 keV antiproton beam to the cryogenic helium target in which $\bar{p}He^+$ atoms were formed (see Fig. 3). Three titanium ion pumps of pumping speed 500 liter/s (Fig. 4(left)), four turbomolecular pumps, and beam apertures and conductance limiters were used to isolate the helium gas target of pressure $P = 0.8$ mb and temperature $T = 1.5$ K from the ultrahigh vacuum in the other parts of the ELENA beamline of $P < 10^{-9}$ mb. This corresponds to a pressure differential of more than 9 orders of magnitude at room temperature.

Three spatial beam profile monitors based on secondary electron emission from a grid of $d = 20$ μm diameter gold-coated tungsten-rhenium wires were positioned along the beamline [59]. One monitor was placed < 300 mm upstream of the $T = 1.5$ K helium target. The monitor contained electrode grids of special design (Fig. 6(left)) that used UHV-compatible gold indium solder. Acrylic and lead-fluoride Cherenkov detectors [60, 61] measured the relative intensities of any loss of antiprotons by collisions with the intermediate apertures or beam pipe.

The beamline was commissioned with both H^- and antiprotons beams in two optical configurations based on the simulations carried out by the CERN TE-ABT-BTP group in a step-by-step manner. Fig. 5(a) shows the horizontal and vertical β-parameters and dispersion σ of the beam envelope along the beamline in the first configuration. The antiprotons were first focused to $\sigma \leq 1$ mm and allowed to pass through an aperture of length $l = 30$ mm and diameter $d = 8$ mm. The
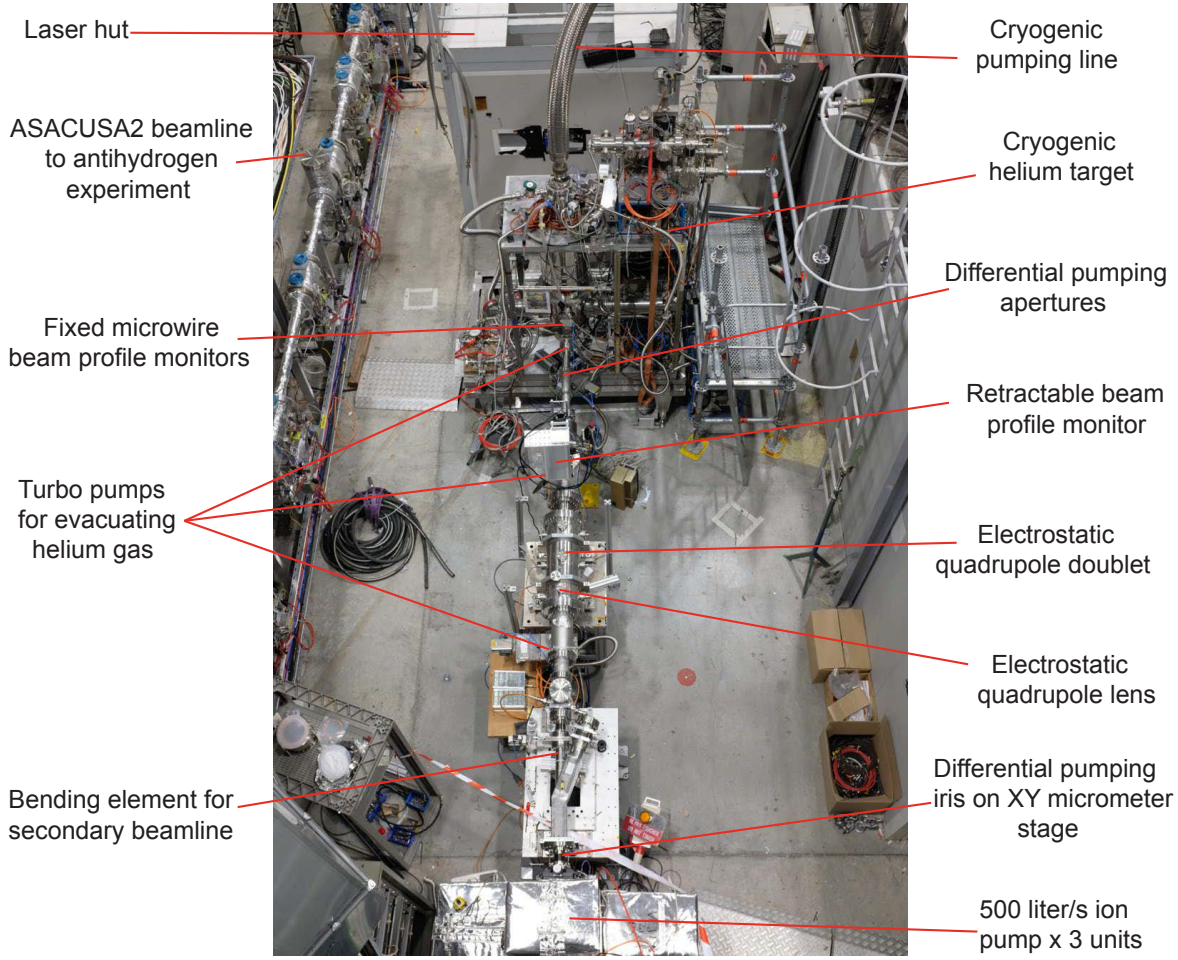
Figure 3 – Top view of the experimental set including the electrostatic beamline and cryogenic helium target constructed by the ASACUSA collaboration during 2021, showing the locations of the pumps and irises for differential pumping, and the profile monitors. Note the cryogenic pumping line at the top of the cryogenic helium target which was modified and installed by the TE-CRG-ME group.

beam rapidly expanded over a distance of 2 m before being refocused by an electrostatic quadrupole triplet of diameter $d = 100$ mm constructed by us. The antiprotons passed through two apertures of diameters $d = 30$ mm and $d = 16$ mm positioned along a 2 m-long beam pipe before being focused to a $d < 3$ mm spot at the entrance polymer window of the target. The window of diameter $d = 6$ mm was fixed to an OFHC copper flange.

We found that the beam traversing the upstream quadrupole lenses had such small β-function values that even minor detunings of a few percent in the voltage settings caused significant changes in the horizontal and vertical focal positions. This caused an excessively large number of antiprotons to annihilate in the outer rim of the 6 mm diameter entrance window of the target. The TE-ABT-BTP group therefore developed a second optical design (Fig. 5(b)) involving larger β-functions at the positions of the upstream lenses, and utilized the three intermediate quadrupole lenses as a modified doublet instead of a triplet. Large improvements in the beam characteristics at the target were seen (Fig. 7). The new design involved a larger beam diameter at the positions of the differential pumping apertures which caused some of the beam to be scrapped and lost.
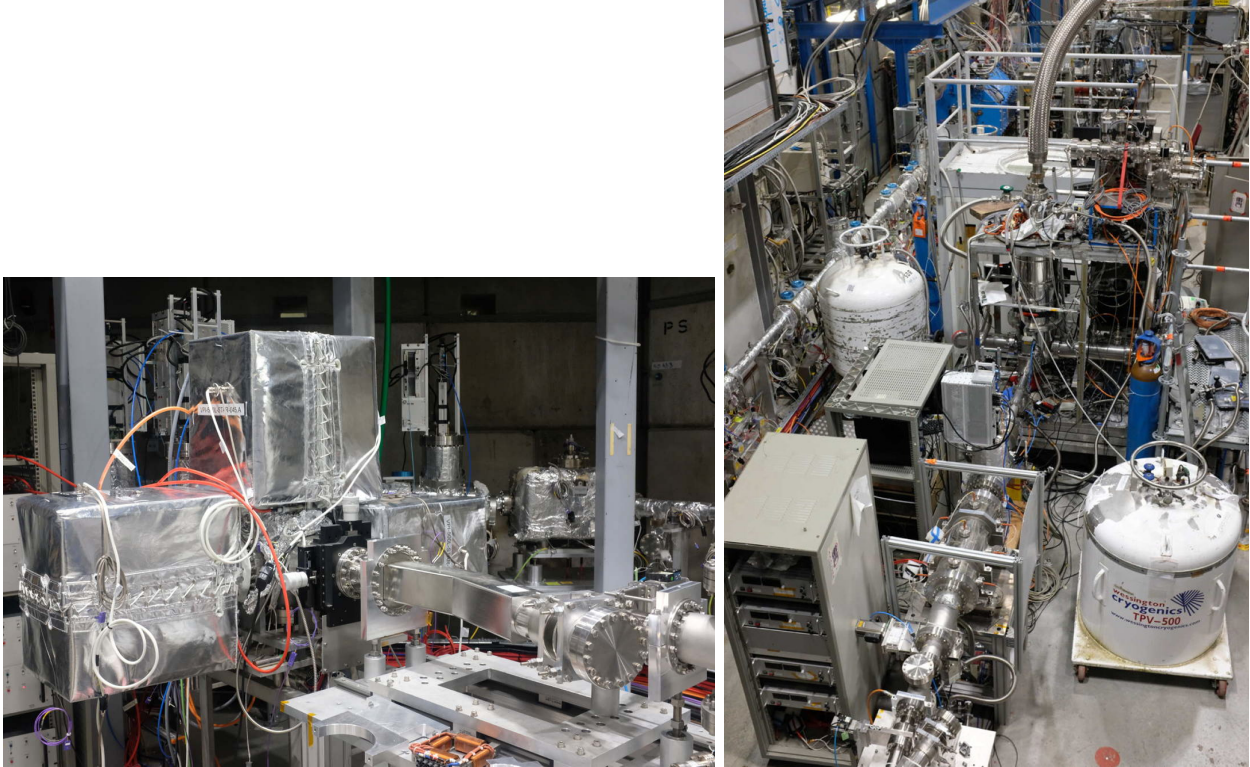
Figure 4 – Differential pumping stage with three 500 liter/sec ion pumps and beam aperture mounted on a XY micrometer stage used to isolate the cryogenic helium target from the ultrahigh vacuum of the ELENA beamline (left). View of cryogenic helium target (right).

Based on this experience, we will install additional electrostatic deflectors and irises of different design in 2022. We are then confident that the first measurements of two-photon laser spectroscopy of $\bar{p}\mathrm{He}^+$ can be carried out using the ELENA beam.

2.2 Cryogenic helium target

A schematic layout of the experimental helium target used in 2021 is shown in Fig. 8, including the spatial configurations of the five laser beams that would eventually be needed to carry out the two-photon laser spectroscopy by a pump-probe method. The TE-CRG-ME group provided valuable support in terms of modifying and installing the cryogenic pumping line (see Fig. 4(right)).

The target chamber contains a pair of cryogenic Brewster windows made of fused silica to admit the laser beams (Fig. 9). In previous experiments, we used similar windows that were sealed using indium and room-temperature vulcanizing silicone sealant. During the beamtime, it was found that small cryogenic leaks appear over repeated cryogenic cyclings that are problematic given the ultrahigh vacuum requirements of ELENA.

In collaboration with the CERN EN-MME-FW group, we are developing a window based on vacuum brazing which is more robustly leak-tight. The titanium vacuum flange that holds the window requires a complex reentrant shape to accommodate the inclined window. As this presented a geometry that could not be manufactured by normal mechanical methods, we used an electric discharge erosion technique. The window was operational at room temperature, but was found to crack during tests at cryogenic temperature due to the slight difference in the thermal expansion
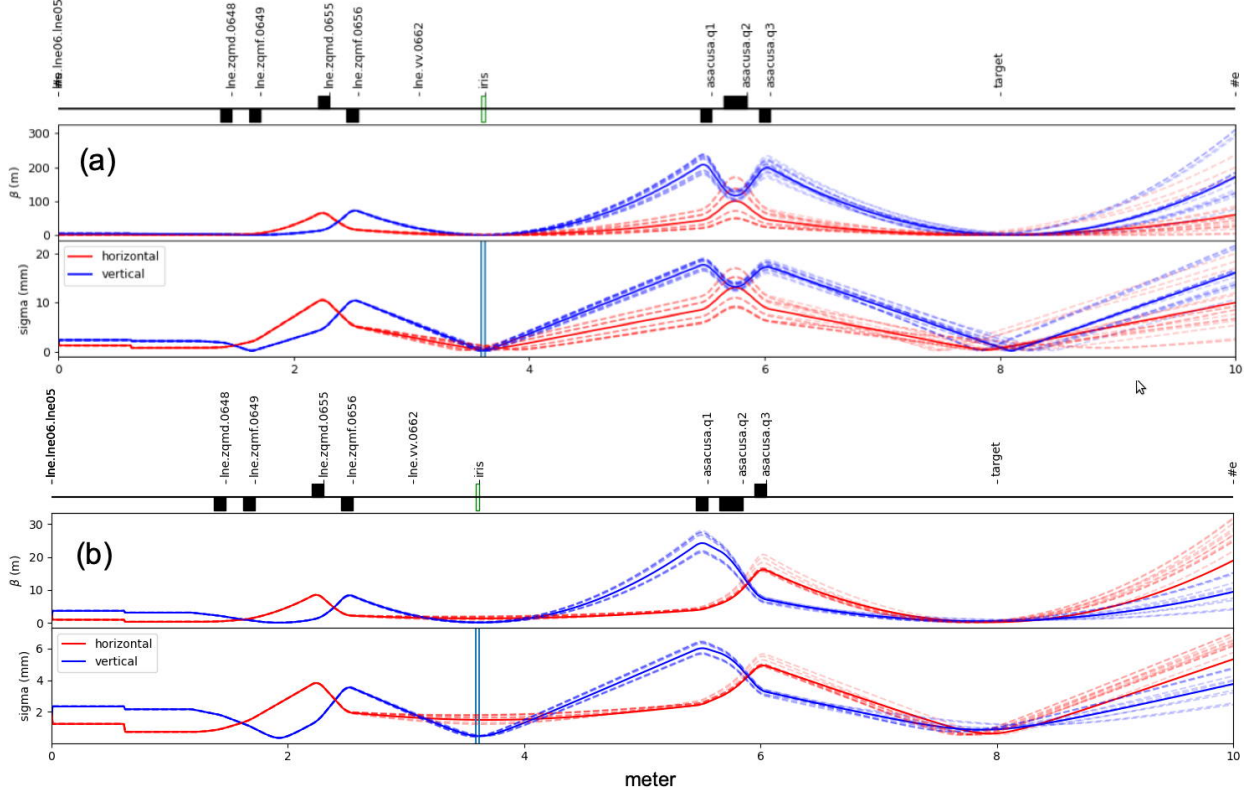
Figure 5 – Two optical designs of the new beamline constructed by ASACUSA and utilized in 2021. (a): The horizontal and vertical β-functions and root-mean-square (RMS) beam size radii of the new beamline simulated by the TE-ABT-BTP group (courtesy, Yann Dutheil). Due to the small value of the β functions at the location of the upstream quadrupole lenses, small changes in the voltages applied to the electrodes caused large shifts in the focal point of the antiproton beam. This made the beamline difficult to precisely tune. (b): New optical design which use the three intermediate quadrupole lenses as a modified doublet, so that the tuning is less sensitive.

coefficients between the titanium flange and the fused silica. An alternative method is now being studied based on a copper flange that is softened by heat treatment in a vacuum furnace.

2.3 MD-RIA calculations of antiproton transmission through polymer foils

Before the features of the cold ELENA beam can be properly utilized in the experiments, the polymer beam window of the cryogenic target which is used to decelerate the antiprotons to keV energies must be carefully optimized. The window also serves as a barrier that separates the cryogenic target gas with the beamline vacuum. Similar polymer or metallic foils are used by the ALPHA, BASE, AEGIS, and ASACUSA-CUSP [62, 63] collaborations, and strongly affect the number of antiprotons that may be trapped. The simulation and design of such windows for MeV antiprotons are well understood since decades, as it was a vital technique for experiments at the LEAR and AD facilities [64]. The far thinner (by a factor of 10^3) deceleration foils at ELENA, however, involves increased sensitivity to processes that occur at keV energies that are insufficiently understood. These processes are not necessarily implemented into the widely-used simulation codes with the high accuracy needed to design an actual experiment. Materials such as Be that can be used for thicker foils are more difficult to precisely machine at 1 μm-scale thicknesses.
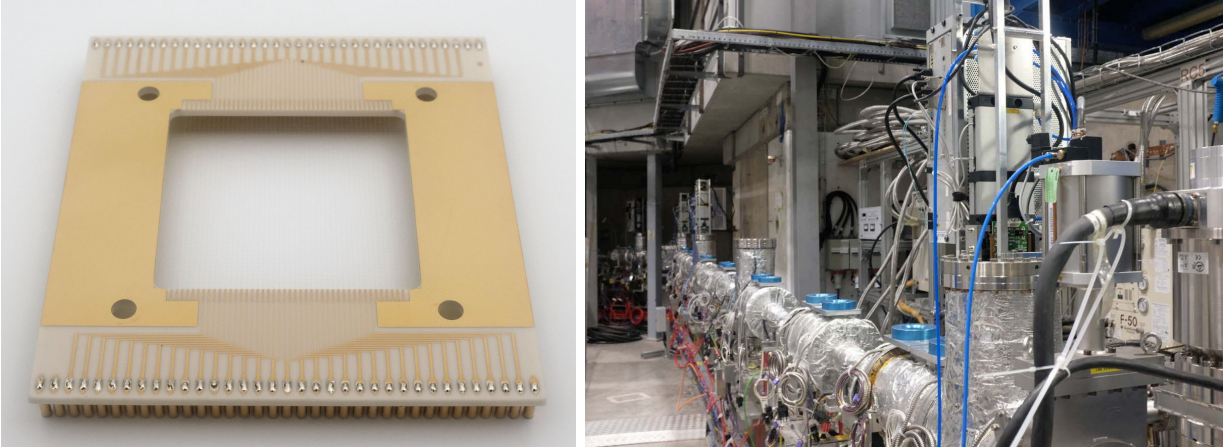
Figure 6 – Electrode of the UHV compatible microwire secondary electron emission monitor of new design positioned 300 mm upstream of the helium target (left). The electrodes needed to complete installation of two of the beam profile monitors of the ASACUSA-2 beamline are now being constructed in Japan (right).
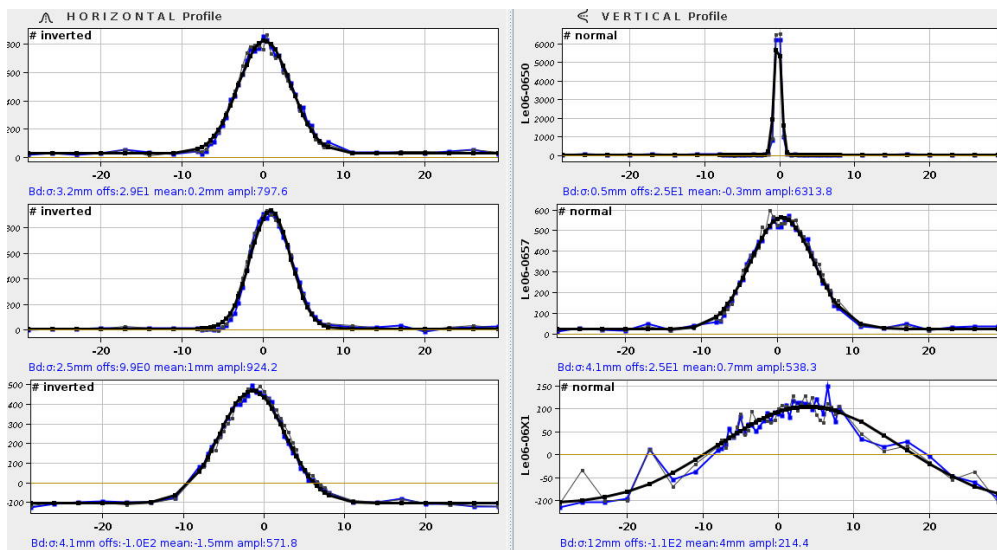
Figure 7 – The horizontal and vertical spatial profiles of the antiproton beam along the new ASACUSA and differential pumping beamlines recorded by the ELENA operations staff. It was found that significant numbers of antiprotons annihilate in an intermediate aperture in the beamline used for differential pumping. We will use a larger aperture and more pumping stages in 2022.

The antiprotons that emerge from the thin foil are broadly distributed between zero and ≈ 15 keV, whereas between 15% and > 60% of the antiprotons typically annihilate in the foil depending on the material used. Among the main reasons for this non-optimal deceleration are the nuclear stopping and elastic scattering [65–71] which are predicted by some theories to become dominant at keV energies just prior to the emission of the antiprotons from the foil. Past theoretical and experimental work (carried out by the OBELIX collaboration of LEAR) of nuclear stopping at such low energies have mostly concentrated on the simplest hydrogen and helium targets.
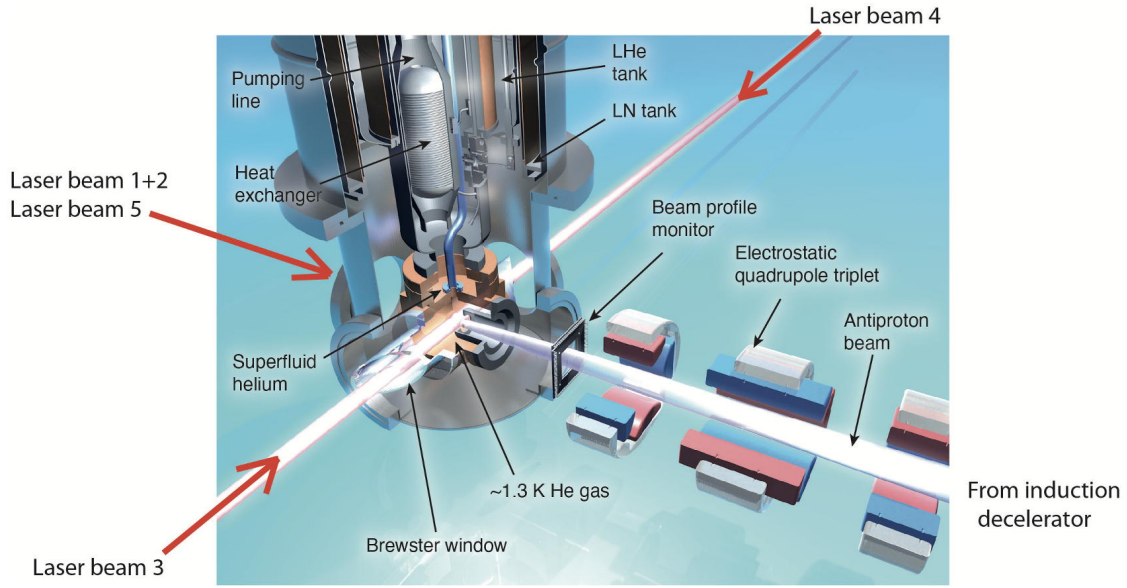
Figure 8 – Schematic drawing of cryogenic helium target with orientation of the five lasers.

Figure 9 – Photographs of new Brewster window made of UV transparent fused silica vacuum brazed to a titanium flange (left). Result after cryogenic cooldown test (right). The window cracked due to the different thermal expansion coefficients which could not be accommodated despite the thin wall of the inclined tube. Other material combinations are now being studied with the CERN EN-MME-FW group. Photograph by CERN EN-MME-FW group.

ASACUSA has measured the annihilation of antiprotons in foils with sub-100 nm and micron-scale thicknesses for many years [63, 72–78]. We found that the results of the GEANT4 code (which is based on sophisticated multiple scattering models optimized for higher particle energies augmented by a single Coulomb scattering model) and SRIM2013 (based on a binary collision approximation which involves the approximately hyperbolic trajectories of positively-charged projectile ions moving in the repulsive ion-atom potential) deviated from our low-energy experimental data, even when the so-called Barkas effect concerning the differences in the electronic stopping
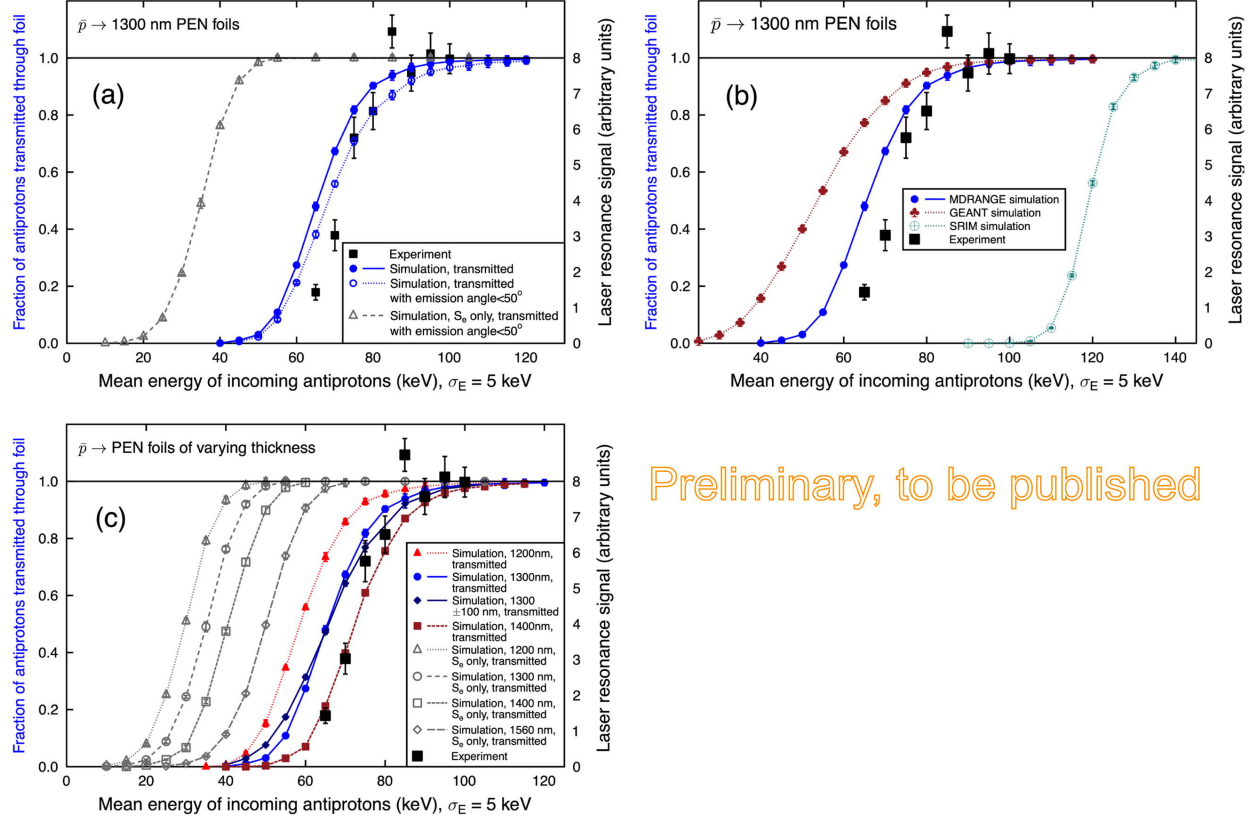
Figure 10 – Simulation results obtained by the Helsinki group in collaboration with ASACUSA in 2021. (a) Relative intensities (filled squares) of antiprotons transmitted through a $t_r = 1300$ nm thick plastic foil of measured by laser spectroscopy of $\bar{p}\text{He}^+$ as a function of the incident beam energy. The results of the MD-RIA simulation with (filled circles) and without (open triangles) nuclear stopping effects, and with a discrimination against antiprotons exiting the foil with an angle $> 50°$ (open circles). (b) Comparisons between the MDRANGE and GEANT4 results for antiprotons, and SRIM2013 for protons. (c) Fractions of the antiprotons that emerged from the foil of uniform thicknesses $t_r = 1200$ nm, 1300 nm, 1400 nm, 1560 nm simulated with and without the nuclear stopping contribution. The results of a simulation in which the foil thickness was varied around the average value $t_r = 1300$ nm by a standard deviation $\sigma_t = 100$ nm are also shown. Preliminary results for the purpose of reporting to SPSC, to be published.

powers of antiprotons and protons was taken into account. This has made it difficult to optimize the foil design in previous years.

As part of the ongoing collaboration with Helsinki researchers [79], the transmission of antiprotons through the polymer and metallic foils were simulated using the molecular dynamics approach in the recoil interaction approximation (MD-RIA) [80, 81]. This multi-body method numerically solves the equations of motion for every simultaneous collision that occurs between the antiproton and multiple atoms in the precise antiproton-atom chemical potential, as the trajectory of the antiproton is tracked within the target. The method is far more computationally intensive and time-consuming compared to other approaches (the simulation of a single experimental condition relevant for ASACUSA using a single core of a modern CPU takes many days to weeks).

Fig. 10(a) shows the relative intensities of antiprotons that traversed the cryogenic $t_r = 1300$ nm thick polymer window and came to rest in the helium target, thereby producing $\bar{p}^4\text{He}^+$. The
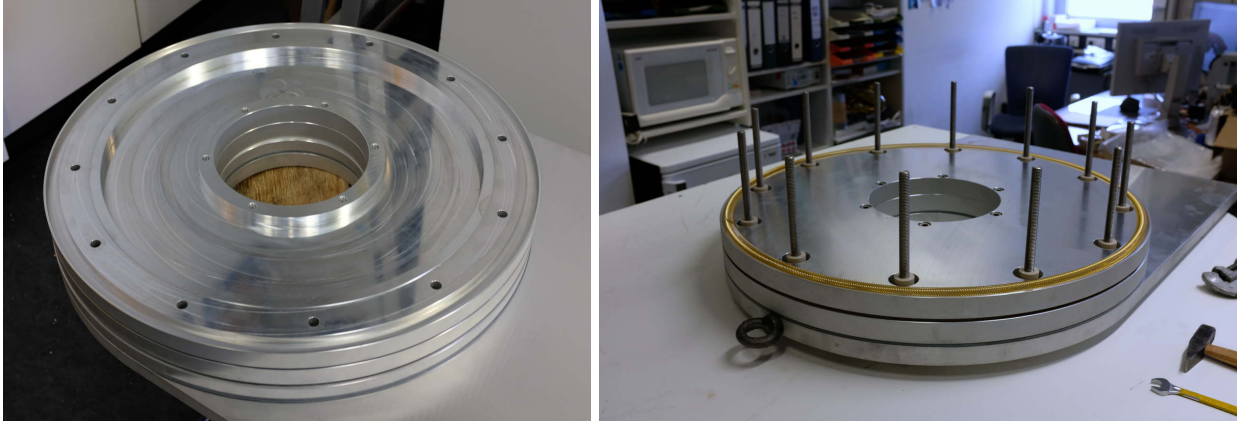
Figure 11 – Parts of the deceleration cells of the induction deceleration under assembly. Gold-coated stainless steel radiofrequency contacts were fitted around the rims of the cells.

intensity of the laser spectroscopic signal [17, 20] was measured as a function of the incident energy $E = 63$–98 keV of the antiproton beam (filled squares with error bars) of the now decommissioned RFQD. A good agreement between the experimental and MD-RIA simulation results (blue solid curve) is seen within the systematic uncertainties of the foil thickness and uniformity. The simulation that includes only the conventional electronic stopping power is a factor ≈ 2 different compared to the experiment. A deviation from the experimental data was seen for the GEANT4 results, while SRIM2013 cannot handle antiprotons so the proton calculations were carried out instead (Fig. 10(b)).

A 200 nm increase in the foil thickness was found to shift the transmission probability curves in terms of the incident beam energy E_k by 10–14 keV, and reduce the transmitted antiproton intensity by up to a factor 2–3 for certain values of E_k (Fig. 10(c)). Conversely, a 200 nm decrease causes the antiprotons to emerge with energies that are too high, so the laser resonance signal would be greatly reduced. The choices of the foil material and surface coatings were found to significantly affect the transmission, as target atoms of high Z elastically scatter antiprotons to larger angles. Even a 25 nm thick layer of Au or Ag coated on the foil surfaces reduced the transmission probability by 40–50%. This work may be of interest to other AD collaborations [82] so we hope to publish soon. Guided by these calculations, in 2021 ASACUSA used a polymer foil of thickness 1.7–1.8 μm in the laser spectroscopy experiments. We thank the ALPHA collaboration, particularly S.S. Fabbri and N. Madsen, for useful discussions.

2.4 Induction decelerator

ASACUSA continued the development of the induction decelerator (see Fig. 11) which would allow the antiproton beam to be slowed down to much lower energies < 40 keV in a highly reproducible way with minimal energy spread and radiated radiofrequency noise. The detrimental effects of decelerating from 100 keV using only a foil can then be reduced and a sample of $\bar{p}\mathrm{He}^+$ atoms of much greater density and small geometric size produced. Cost and design optimizations were carried out based on the experience with the ELENA beam in 2021. The use of SiC MOSFETs of greater voltage amplitude than before simplified the circuit design. Refinements to the prototype device are being continued, while funding for the full deceleration device based on the beam measurements of 2021 has been requested in Germany.

As shown in the laser spectroscopic data of Fig. 10, reducing the beam energy to $E = 70 - 80$ keV in steps of 5 keV by biasing the electrodes of the RFQD was necessary to ensure that the greatest number of antiprotons came to rest in the laser beam in a highly sensitive way. Only then could the two-photon signal be observed with the highest signal-to-noise ratio. Simulations based on the 2021 experience show that far better conditions would be achieved if the induction decelerator slowed down the antiprotons to $E < 30 - 40$ keV prior to the arrival at the target window; we would then expect a): a factor > 20 increase in the annual data collection, and b): a signal-to-noise ratio which is a factor 2-6 greater compared to previous experiments using the RFQD. Any spurious component of the partially decelerated antiprotons would present a high background contamination and would become a source of systematic uncertainty. Thus the high stability afforded by the induction decelerator design is vital for this precision experiment.

3 Publications related to antiprotonic helium

A major upcoming publication for ASACUSA involves the unexpected behaviour in the laser resonance spectra of $\overline{p}\mathrm{He}^+$ atoms implanted in superfluid, liquid, and supercritical phase helium targets. During 2021 the paper was very carefully prepared and it will soon be published [22]. The study may provide information about the microscopic properties of superfluid using antiprotons as probes, which may augment conventional experiments that utilize neutrons or muons. The theoretical group of the INRNE laboratory in Sofia is carrying out quantum chemical calculations of antiprotonic and pionic helium atoms [21, 83, 84] suspended in superfluid helium. Other publications regarding high-precision spectroscopy, and highly-excited states of the atom are under preparation.

4 Preparations for the 2022 beamtime

4.1 Two-photon transitions in the first phase of ELENA experiments

In 2022, we intend to concentrate our efforts on the laser spectroscopy of the four most intense two-photon transitions [15,25] $(n, \ell) \rightarrow (n-2, \ell-2)$ of the $\overline{p}^3\mathrm{He}^+$ and $\overline{p}^4\mathrm{He}^+$ isotopes. The two laser systems needed for this measurement are ready. The transition frequencies have been calculated to a fractional precision of $(5-6) \times 10^{-11}$ [3,4] which corresponds to a sensitivity to the antiproton-to-electron mass ratio of less than 4 parts in 10^{-11}. Based on the experience of 2021, we expect that the cooled beam of ELENA allows up to an order-of-magnitude increase in the number of $\overline{p}\mathrm{He}^+$ atoms produced per year; this will allow various systematic effects to be studied. The numerous upgrades in the beamline mentioned above will be implemented to achieve this. We also intend to study the electromagnetic cascade effects of $\overline{p}\mathrm{He}^+$ [19, 85–87].

4.2 Beam profile monitors for ELENA

During 2018–2021 we provided the parts for 43 monitors that measure the spatial profiles of the antiproton and H^- beams in the injection, ejection, and user beamlines of ELENA. The semi-non-destructive nature of the monitor allowed the four antiproton beam pulses of ELENA to be distributed to four user experiments simultaneously in an efficient and reliable way. The device detects femtocoulomb-scale electric charge induced by the small fraction of antiprotons intercepted by a grid of wires with a diameter of $d = 20$ μm [59].

The ELENA construction, beam diagnostics, vacuum, and other expert groups carried out the assembly, validation, installation, and modifications of the devices. The monitor commissioning in 2021 with antiprotons proceeded smoothly. All the technical information needed for monitor

maintenance have been transferred to CERN, except for the manufacture of the sensor grids which are carried out in Japan.

We have previously reported on the issue of some of the fluxless soldering on the signal pins of the monitors becoming disconnected during the 3 days baking at temperatures of $T = 180 - 200$ °C at CERN. The problem is related to leeching in the solder connection. In Japan, tests with adhesives and gold nanoparticles were carried out to repair the sensor grids. As of December 2021, the following 5 electrode sets are still missing (see Fig. 6(right)) and must be delivered by ASACUSA before the project can be fully completed,

- 1 fixed monitor for **BASE-STEP** now under construction.

- 1 fixed monitor for **PUMA**.

- 3 standard monitors for replacement in **ASACUSA-1 and 2**.

The grid repairs are ongoing and the 5 missing units will be sent to CERN soon. We again deeply thank the CERN accelerator groups for their great efforts and support on this project.

4.3 Laser systems and optical reference signals from metrological institutions to CERN

In 2021 the collaboration continued construction of the three additional sets of Nd:YAG-pumped injection-seeded Ti:sapphire lasers, which (together with the two existing lasers) are needed to provide the five laser beams for the pump-probe experiment [20, 88]. Similar lasers have recently demonstrated an Allan deviation of 5×10^{-11} at a 10 second integration time relative to a continuous wave laser [89]. The optical frequencies of the continuous-wave lasers which seed the pulsed amplifiers that probe the $\overline{p}\mathrm{He}^+$ atoms will be measured by an Er femtosecond frequency comb, which will be referenced to a hydrogen maser. For the 2022–2023 experiments, the maser will be referenced to a Global Positioning Satellite (GPS) receiver.

In the experiment, a pulsed beam of antiprotons arrives at intervals of 120 s, which also defines the repetition rate of the data acquisition. A measurement of a laser resonance thus takes many weeks of data accumulation at 120 s intervals. The maser guarantees the stability of the optical frequency measurements over the relevant time scales. We have requested funding to purchase a hydrogen maser. In the meantime, we will utilize an alternative system that uses the GPS reference signal to directly stabilize a quartz oscillator, while simultaneously using two Rb atomic clocks as secondary references.

In 2021 the SNF-Sinergia research project between the University of Basel, ETH Zürich, METAS, and the Swiss national research and education network SWITCH published a paper which presented the performance of the 456 km-long fiber link that carried an ultrastable optical frequency standard signal [90]. METAS operates an active hydrogen maser referenced to a two-way satellite time and frequency transfer (TWSTFT), and the Swiss Cs continuous primary frequency standard FoCS-2 (Fontaine Continue Suisse) which achieves a relative uncertainty of 1.99×10^{-15} and a short-term stability of 8×10^{-14} at an integration time of 1 second [91]. An optical signal referenced to these frequency standards was sent from Bern to ETH and Basel without interruption for several days. The optical phase noise was evaluated and a link instability of 4.7×10^{-16} at 1 s and 3.8×10^{-19} at 2000 s integration time, and a link accuracy of 2×10^{-18} was demonstrated (see Fig. 13). The technology utilizes a so-called "dark channel" (ITU CH07) corresponding to a wavelength $\lambda = 1572$ nm. This allows the reference signal to be transmitted parasitically on existing data fibers administered by SWITCH that connect Bern to CERN.
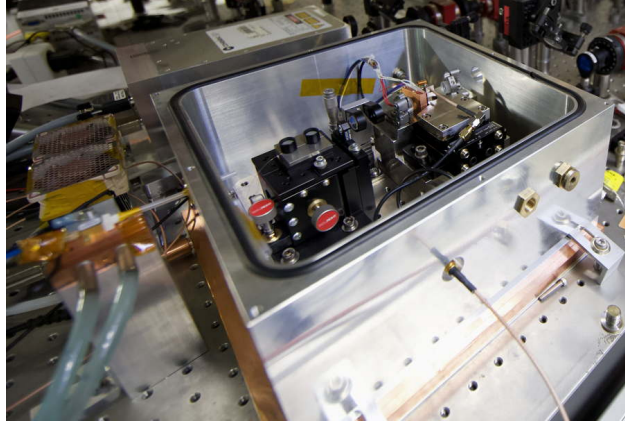
Figure 12 – Photograph of one of the oscillators of the Nd:YAG pump lasers used for laser spectroscopy of $\overline{p}\mathrm{He}^+$.
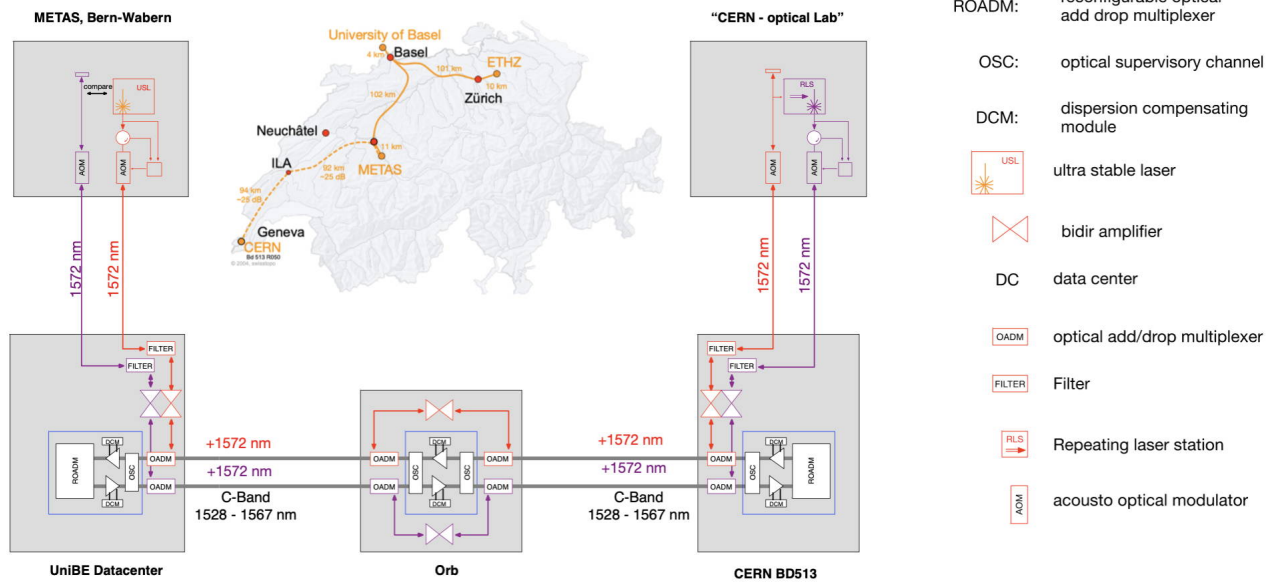
Figure 13 – Geographical and schematic layout of the fiber link between Bern and CERN to transfer the ultrastable optical reference signal, as proposed in spring of 2021. In early 2022 a new proposal to construct a ring topology with univerisites of Neuchatel and Geneva, CERN, EPFL, and other possible users was proposed. Figures courtesy of SWITCH and METAS.

The $\overline{p}\mathrm{He}^+$ experiment hopes to participate in this effort as a client user. The optical reference signal will arrive at the CERN computer center and transmitted to Bat. 193 via optical fibers that will be newly installed. As mentioned above, the measurements of $\overline{p}\mathrm{He}^+$ can only be carried out every 120 seconds, during short time intervals of ≈ 10 μs which are defined by the lifetime of the exotic atom. Data from multiple measurements over many months must be added together, so both the long and short-term stability of the frequency reference are vitally important. Our

discussions with experts showed that the fiber link would be a valuable way to test the accuracy of our measurements.

Discussions between ALPHA, ASACUSA, SWITCH, METAS, and the universities of Basel and Geneva explored the possibilities of this CERN extension. Talks were continued between CERN IT department, fiber installation experts, and the CERN Quantum Technology Initiative (CERN-QTI). In December, the universities spearheaded the Swiss Quantum Communication Infrastructure (Swiss-QCI) proposal to construct among other things a ring topology network that connects METAS with Neuchatel, Geneva, CERN, CSEM, EPFL, and other commercial users. This would facilitate research in precision atomic and molecular spectroscopy, quantum sensing, and quantum communication in these institutions. The French NREN RENATER and the Polish research institutes plan to also send an ultrastable fiber signal from Observatorie de Paris and Poznan to CERN, as mentioned in a previous status report.

Part II
Antihydrogen

As described in the previous report to the SPSC, the ASACUSA antihydrogen experiment had ambitious plans for 2021. This included replacing the positron accumulation apparatus, the Cusp trap and cold bore, and installing a new drift tube accelerator which would make our antiproton trap MUSASHI compatible with the new ELENA beam. As will be discussed in the coming sections, these plans were mostly realised albeit not to the schedule we desired. The ongoing pandemic situation during 2021 disrupted our ability to bring personnel to CERN, affected the ability of manufacturers to keep to schedules, and interfered with supply lines all of which caused delays.

Despite these setbacks, at the end of 2021 we find ourselves in a very strong position going into 2022. The new drift tube accelerator was successfully operated with the MUSASHI trap, allowing a large number of antiprotons to be stored ($\sim$ 1 million per shot). The new Cusp trap is installed in the area with electrodes 10 K cooler than previously possible. Our systematic studies of plasma properties have allowed us to produce plasmas of millions of electrons cooled to 25 K with cyclotron cooling alone, 100 K colder than our previous best. Our new positron accumulator has been installed and successfully trapped particles beginning the process of fully integrating into our systems.

In the coming year we will build upon these successes, catching positrons and antiprotons in the Cusp trap and beginning the work on optimising our antihydrogen production for beam formation. Unfortunately, as we begin 2022 we are in a very similar situation to 2021 with a new Covid variant blocking travel and causing delays. However, we hope to be as productive in the new year as the last closing in on our goal of measuring the hyperfine structure of antihydrogen in a field free region.

5   Antiprotons

5.1   Antiproton trapping in MUSASHI

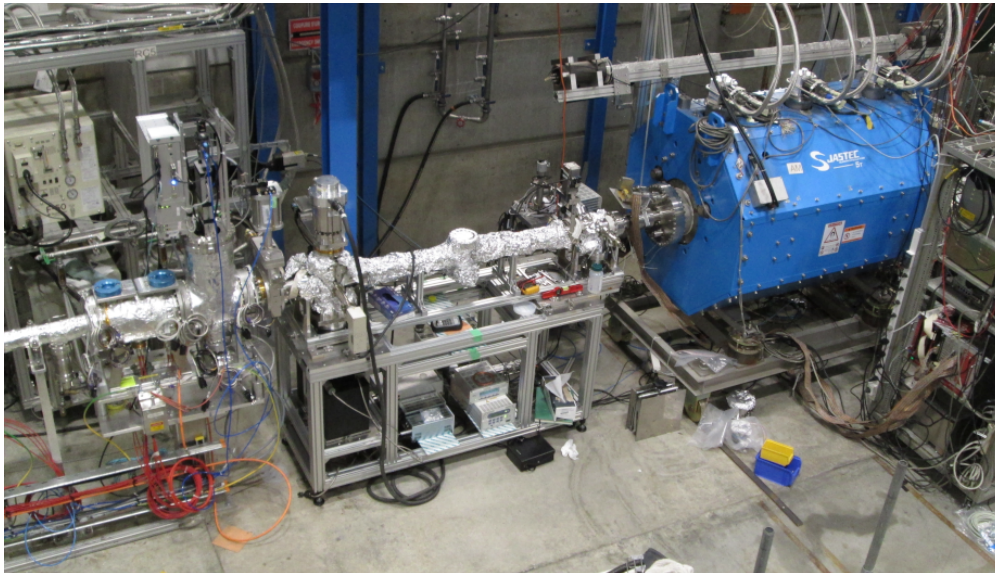**Figure 14** – The drift tube beam energy adjuster
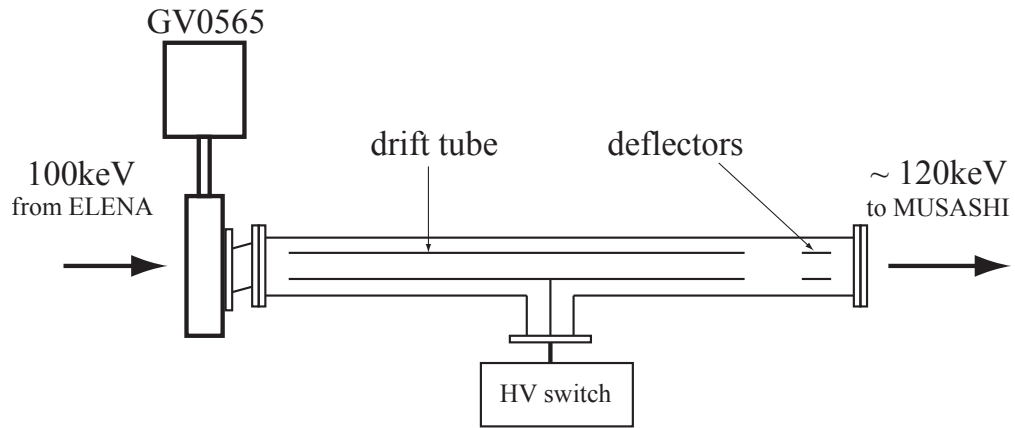
Figure 15 – Schematic view of the drift tube (not to scale)
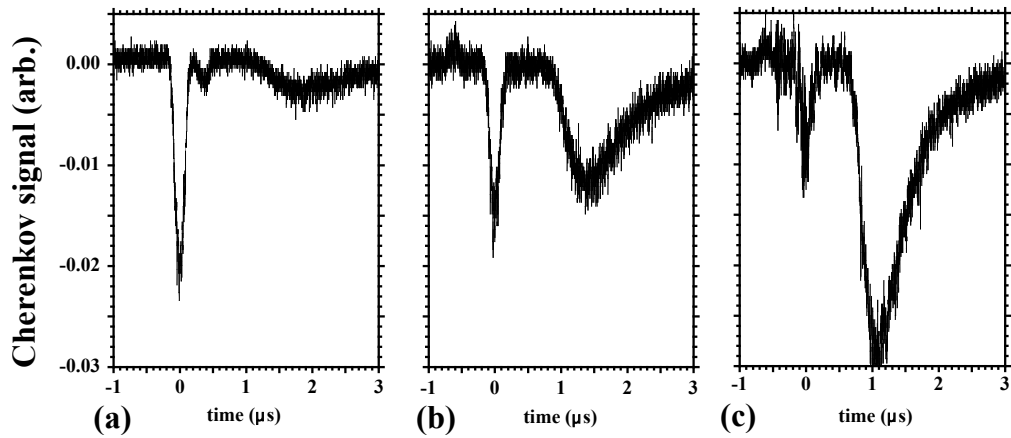
Figure 16 – Čerenkov signals. (a) $\phi = 0\,\mathrm{kV}$, (b) $\phi = -10\,\mathrm{kV}$, (c) $\phi = -20\,\mathrm{kV}$.
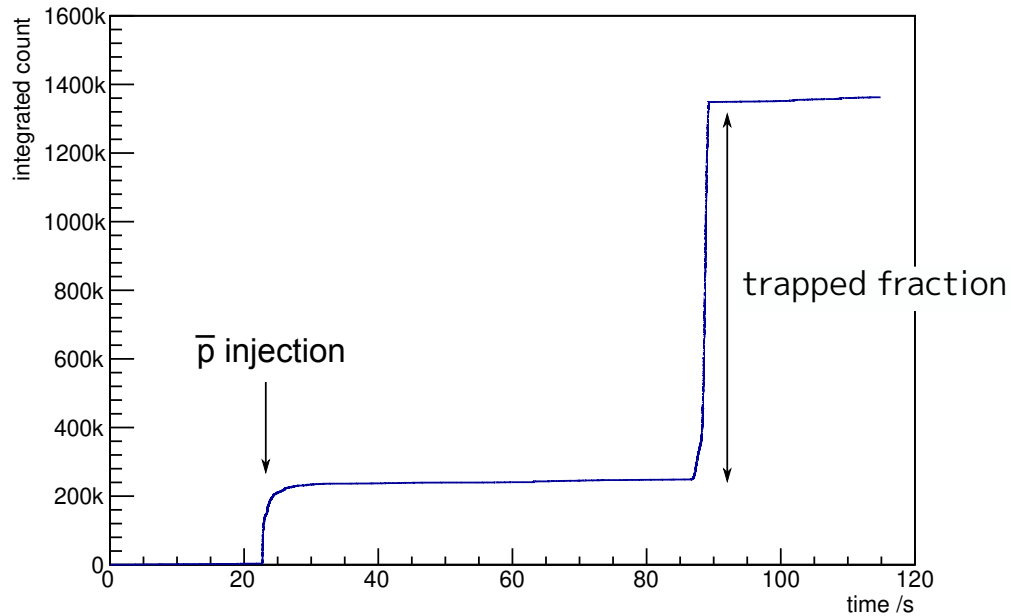

Figure 17 – Counts of $\bar{\mathrm{p}}$ annihilation during one cycle of capture, cool, and release. More than 1.1 million $\bar{\mathrm{p}}$ were trapped.

17

A drift-tube type beam energy adjuster was developed to bridge the gap between ELENA's LNE05 antiproton beamline and the MUSASHI trap of the ASACUSA-Cusp experiment. The MUSASHI trap is equipped with thin Bo-PET foils that function as both a beam profile monitors and an energy moderators. The foil monitor is capable of detecting fine adjustments during beam steering in the AD-RFQD era [92]. However, as 120 keV beam energy was the optimum for the foil, an energy adjuster for the antiproton beam from ELENA was required to take advantage of this beam profile monitor.

Fig. 14 shows the drift-tube energy adjuster installed between the LNE05 beamline and the MUSASHI trap. As shown in Fig. 15, a cylindrical aluminium electrode with a length of 1.5 m is used to accelerate the beam. In one bunch more than 95% of antiprotons can gain 20 keV, according to the ELENA design value of the bunch length, $\sigma = 75$ ns. In addition, there is a set of beam deflectors downstream of the electrode to allow further steering.

Thanks to the AD/ELENA team's tireless efforts, antiproton beams have been available for the MUSASHI trap of the ASACUSA CUSP experiment from the end of August 2021. We installed a Čerenkov detector at the exit of the MUSASHI trap. Fig. 16 shows the outputs of the detector. The first peak around $t = 0$ µs corresponds to annihilation at the PET foil. When the potential at the drift tube (ϕ) was increased, the peak decreased and we observed an increase in the decelerated component around $t = 1$–2 µs.

Thus, the drift tube energy adjuster was observed to successfully function, hence, more than one million antiprotons per bunch were trapped during the period when the ELENA Vistar stably showed > 7 million $\bar{p}$ (See. Fig. 17).

Unfortunately, further optimisation could not be performed. Four SEMs in LNE05 after the last bending element were expected to locate the beam. However, only two SEMs were in operation. It was challenging to adjust the beam under these limited conditions. Further to this, it was very difficult to follow the significant changes in the beam transport conditions that occurred, at least twice, during the beamtime. For example, a sudden change in beam conditions from AD/ELENA just before the final day of beam time did not allow us to recover the trapped number. According to correspondance with the AD/ELENA team, the missing two SEMs will be in operation in 2022. In addition, there is a vertical misalignment of approximatly 9 mm at the hand-over point as schematically shown in Fig. 15. The last SEM provided a shifted beam profile when we observed the record-high number of antiprotons in the MUSASHI trap with ELENA.

For the coming beamtime in 2022, the MUSASHI trap will confine more antiprotons by improving the above issues, leading to more antiprotons and thus antihydrogen atoms produced in the double cusp trap.

5.2 Upgrade of the scintillating bar detector

The goal of the scintillating bar detector is to determine the time and the vertex position of the antiproton/antihydrogen annihilations by detecting the charged annihilation pions. It consists of 8 planes made of different number of scintillating bars (from 30 to 60) with an active surface from 0.5 m^2 to 1 m^2. They are usually coupled in 4 "X-Y" modules to determine 3D tracks, but they can be placed separately to increase the solid angle coverage.

The scintillation light is carried out by WLS fibers that in the previous version were grouped and read out by 64-anode PMTs. During LS2, the light readout system has been upgraded as planned and the PMTs have been replaced with SiPMs in a 1-to-1 configuration (each channel is read out by a single SiPM). The SiPMs are ASD-RGB1S-P-40 by FBK with 1×1 mm^2 active surfaces composed of 625 micro-cells of 40 μm. The upgrade was performed in the following steps:
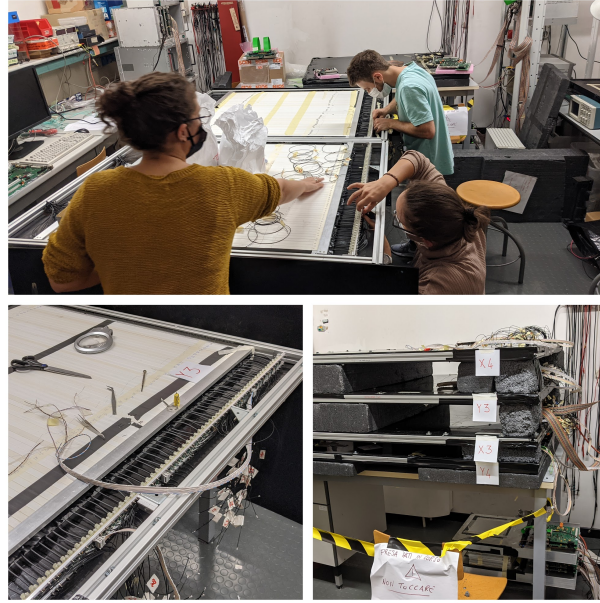
Figure 18 – Assembly of the scintillating bars planes in the lab and their final stacking for the test run. Below the planes, a silicon microstrip detector tracks the traversing cosmic rays. Two scintillating counters are used to trigger the system.

- the fibers were shortened, polished, and new optical couplers were produced by a high resolution 3D printer to connect each fiber to a single SiPM;

- two new front-end boards have been designed and produced to read out the SiPMs signals and carry them to the current readout board based on the MAROC3 chip (for a more detailed description of the DAQ electronics, which has not changed, see [93]);

- the mechanical supports and internal frames of the planes have been refurbished to cope with the new layout.

The detector new front-end boards have been tested and the SiPMs readout system validated. Eight planes have been completed and underwent preliminary tests with cosmic rays with the main purpose to investigate the efficiency and light yield uniformity across each plane, and to spot any assembly defect. Fig. 18 shows one of the planes during the assembly phase.

6   Electrons

Antihydrogen will be formed by mixing cold antiprotons and positrons in the Cusp trap. The trap was modified several times in 2021 (Section 6.1). After each modification, the trap was commissioned using electrons (Section 6.2). Electron plasma can be held stably in the Cusp field with typical expansion time $\tau \sim 1000\,\mathrm{s}$. The plasma can be cooled passively to a temperature $T \approx 25\,\mathrm{K}$ over a wide range of plasma density n and particle number N. The plasma can be cooled further to $T \approx 10\,\mathrm{K}$ by "evaporative cooling" [94], while maintaining a density and total particle number similar to those reported by the ALPHA collaboration for their standard mixing routine [95]. These temperatures are among the lowest yet reported for nonneutral plasma, nearly an order of magnitude lower than what has been previously achieved in the Cusp trap. Assuming

that these results can be reproduced in 2022, for plasma composed of positrons instead of electrons, the corresponding ground state antihydrogen yield after mixing is expected to increase by two orders of magnitude [96] relative to what was reported in 2021 [97].

6.1 Upgrades to the Cusp Trap

As discussed in the previous SPSC report, there was a staggered upgrading of the Cusp trap during 2021. This began in January with the installation of a new set of the trap electrodes in the existing cold bore (see [98]). Further interventions occurred during the summer as part of a study of the radiation environment in the trap (see Section 6.2). During the autumn, a complete upgrade of the cold bore was performed incorporating the new and now tested electrode stack design.
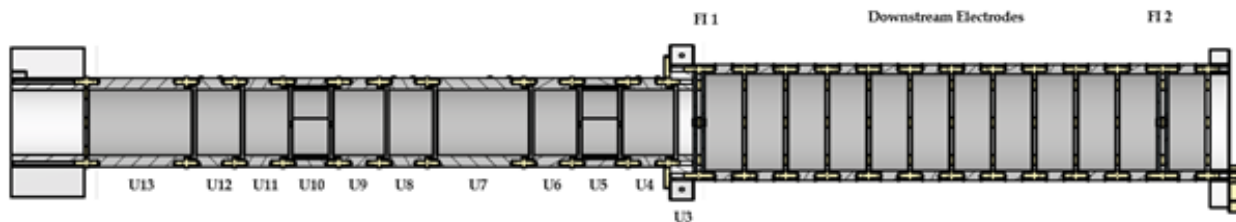

Figure 19 – A schematic diagram of the new electrode configuration. U13 is the pulsed catching electrode, U10, and U5 are split into 4 petals to allow the application of a rotating wall electric field.

The intervention in January saw the installation of the new design electrode stack. This stack reduced the electrode diameter from 80 mm to 34 mm in the mixing region where antihydrogen is produced (the downstream electrodes increased in diameter marginally from 48 mm to 50 mm). Single width electrodes are 25 mm in length and have a 2 mm insulation gap between them. As the electrode stack is a common feature between both the upgrades of this year, Fig. 19 shows a drawing of the final arrangement for 2021. In both stacks, U13 was used as a pulsed electrode for catching, U10 and U5 were split into 4 sectors to allow the application of a rotating wall electric field [99], and U7 was a double length electrode. The electrodes were manufactured from aluminium and gold coated; a thin layer of colloidal graphite was then applied to the internal surfaces, this has the beneficial effect of absorbing light, reducing variation in surface potentials, and increasing the cryo-pumping area.

The downstream electrodes are tied together via a resistor chain and house two pairs of independently biased field ionizer grids (see Fig. 19). These electrodes are 50 mm in diameter and 19.5 mm long and prepared in the same way as the upstream electrodes. The field ionizer grids were etched from beryllium copper and again coated with a thin colloidal graphite layer (see Fig. 20). They are designed to have a high transparency (97 %) whilst being mechanically stable under the application of $\sim$ kV potential differences. One significant difference between the final design shown in Fig. 19 and the stack installed in January was the downstream electrodes, in this case only the first field ionizer was installed and the stack shortened accordingly.

During this intervention, the broken cold head was disconnected from the cold bore which reduced the electrode temperature from the 70 K achieved in 2021 to 35 K. An externally controlled downstream thermal shield, which was used in a previous configuration of the Cusp trap [100], was also installed. The inclusion of this shield allowed us to perform systematic tests of the effect of changing the thermal environment visible to the plasma. With the shield closed, the plasma was

Figure 20 – A photograph of the field ionizer grids. The top two grids are visible in this photograph, the second can be seen by closely examining the upper right hand quadrant.

exposed to the 200 K radiation from the door, shield open the room temperature region beyond the cold bore was visible.

Aside from the work on the cold bore and electrodes, as discussed previously [98], the upstream plasma detector was upgraded replacing the old chevron arrangement MCP stack with a single 0.5 mm Hammamatsu MCP coupled to a fast (80 ns) decay time phosphor screen.

In August the plasma experiments were stopped in order to begin the installation of the new cold bore. This involved removing all existing chambers and equipment, stripping the apparatus back to just the double Cusp magnet and frame. This work was performed outside of the ASACUSA area to allow studies with antiprotons to continue unhindered. As discussed in more detail in the last report, the new design incorporates the electrode stack at the heart of the cold bore.
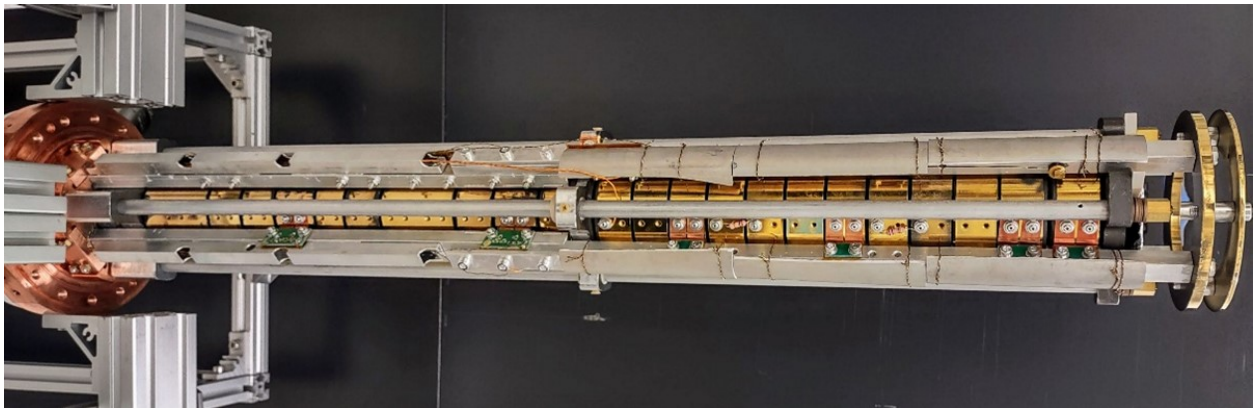
Figure 21 – Photograph of the new electrode stack. The large copper flange is visible on the LHS of the image connected to an Al profile mount. Wiring conduit and electronic filter boards are connected to annealed 5N Al bars on the upstream side of the trap. On the downstream side, ceramics coated with thin metallic layer are tied onto the bars. Two baffles are visible at the exit of the trap.

A photograph of the electrode stack can be seen in Fig. 21. Briefly, the trap is constructed onto

a large block of oxygen free copper, heat is transferred from the electrodes to the copper block via connections to electronic noise filter boards which are mounted securely on annealed 5N Al rods sunk to the main copper flange (see Fig. 22).
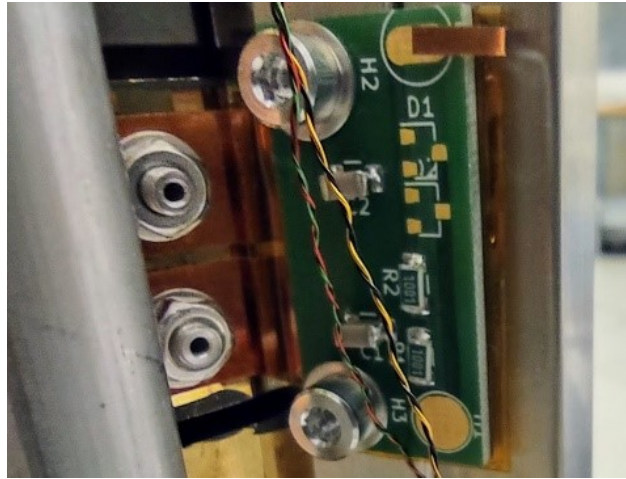
Figure 22 – Photograph showing the thermal and electrical connection between electrode and filter board. A thin copper connection (insulated where needed using Kapton) is pressed between the filter and the 5N Al bar, then secured to the electrode.

The ultra-high vacuum chamber (UHV) is constructed from Al and connects directly to the main Cu flange sealed with an indium ring, this provides both good thermal contact, and vacuum. Connection to room temperature sections was made using bellows to provide a long thermal path between the 4K and 40K, then 40K and 300K regions (see Fig. 23). The interior of all the inner vacuum vessels was again coated with a thin layer of colloidal graphite.

To block incoming microwaves, copper meshes (0.25 mm pitch, 0.03 mm wire diameter) were installed at the entrance to the trap, and the exit of the UHV (see Fig. 24). To absorb microwaves produced by the plasma, stainless steel inserts were placed into the UHV and ceramics with a thin conducting layer (see Fig. 21) were tied to the 5N Al bars on the downstream side of the trap [101] (more details below).

The OVC chambers were a source of delay in construction of the new cold bore, although expected to arrive in late August, the manufacturers VACOM continued to push the delivery date back due to delays in their factory. The chambers eventually arrived at CERN in early October.

By the middle of October, the inner chambers were mounted in the OVC. The mounting system is another significant change between this new cold bore and the previous design. Previously only X,Y alignment was possible and connection to the cold inner parts was made via large PTFE blocks. In the new model X,Y and Z alignment is possible and connection is made via Kevlar strings tied in loops (see Fig. 25).

The Cusp trap was moved back into the area at the end of October and reconnected to MUSASHI and the positron system, baking of the entire apparatus then begun. Once baked, the UHV was connected to the cryocoolers (RDE-418D4 and RDK-408D2 from Sumitomo) using thin strips of annealed 5N aluminium, and cooled. The electrode stack reached a temperature of around 6 K on the 13th of November, 2 days before the end of beam time. There was not enough time left to work with antiprotons in the new Cusp trap this year. However, this temperature is 10 K colder than the previous best temperature achieved by ASACUSA.
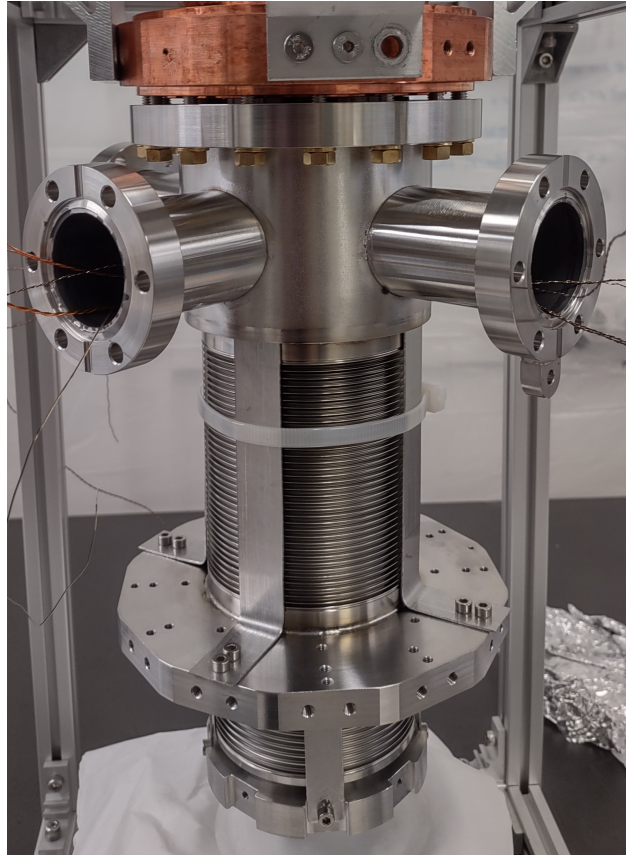
Figure 23 – Photograph showing the upstream bellows used to connect to 300 K (bottom flange), 40 K (middle flange) and 4 K (mounted to Cu block) stages. In this image the bellows are extended with stretcher bars to allow painting of the interior with colloidal graphite. Wiring from the trap can be seen before the connection of multi-pin feed through.
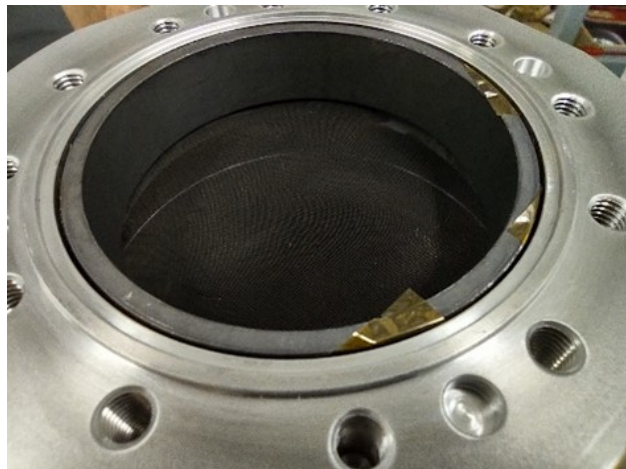

Figure 24 – Mesh on the exit of the inner vacuum chamber, the visible Kapton tape was later removed.

Figure 25 – LHS shows a photograph of the PTFE blocks used in the previous cold bore design compared on the right to the Kevlar string used in the present design.

6.2 Electron Plasma Temperature

Control over plasma parameters such as radius and number of particles at the 1% level was demonstrated in our previous report to the SPSC. At that time, the lowest plasma temperature achievable without evaporative cooling was around $T_f = 130\,\mathrm{K}$, in a trap cooled to $T_t = 70\,\mathrm{K}$. Roughly half of the difference between T_f and T_t was attributed to heating from plasma expansion. Since then, improvements to trap alignment have also permitted a reduction of the plasma expansion rate. Surprisingly, reducing the plasma expansion rate did not significantly alter the minimum attainable plasma temperature. Low temperature ($T_f < 30\,\mathrm{K}$) was finally achieved near the end of the 2021 run, after a meticulous investigation of other possible heating sources involving several iterative modifications to the Cusp trap.

Nonneutral plasma is heated primarily by noise on the confining electrodes and self-repulsion during plasma expansion. The use of *in situ* cryogenic low-pass filters should result in superior noise reduction in the Cusp trap, compared to other traps in the AD and elsewhere. Improvements to trap alignment undertaken early in 2021 eliminated expansion as a major heating source for plasma having density $n < 3 \times 10^8\,\mathrm{cm}^{-3}$ and radius $r_p < 1\,\mathrm{mm}$. Indeed, it was found that the plasma with the lowest temperature, $T_f \approx 150\,\mathrm{K}$ at the time, was not any hotter if the density was increased by a factor of three (This was no doubt due to the very low expansion rate, $\nu = 1.4 \times 10^{-4}\,\mathrm{s}^{-1}$, and high cooling rate, $\Gamma \approx 0.9\,\mathrm{s}^{-1}$, due to the plasma being held at the maximum of the Cusp magnetic field.). Further, the plasma was insensitive to broadband radiofrequency noise injected on various lines leading into the trap, implying that the cryogenic filters were preventing such noise from reaching the confining electrodes.

Why was the plasma so much hotter than the electrodes, then? The clue came from a study using a movable thermal shield, which was re-installed on the downstream side of the trap. It was found that T_f was consistently $20\,\mathrm{K}$ higher when the shield was open. The magnitude of the effect was the same independent of the amount of time the shield was open (a few seconds up to several hours) or the number of particles in the plasma ($2.5 < N < 12 \times 10^6$ electrons). In addition, an intermediate "partly open" position was found for which the temperature excess was not 20 but $10\,\mathrm{K}$. This position did not permit a line-of-sight path into the trap. The preferred hypothesis was that the shield partially blocked microwave radiation entering from outside the cryogenic region, which effectively raises the temperature of the thermal bath seen by the plasma (for a more detailed
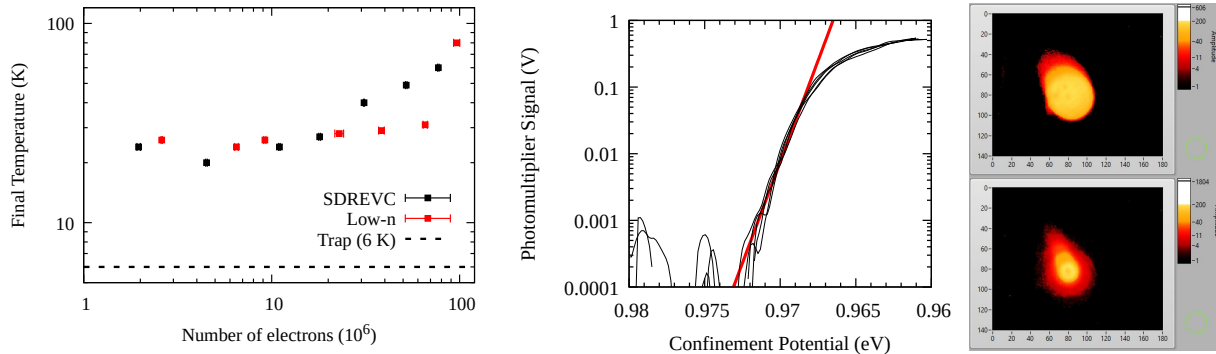
Figure 26 – Evidence for low plasma temperature achieved in the new cold bore with copper meshes. Left: Steady-state plasma temperature as a function of number of electrons N. The series "Low-n" corresponds to a plasma prepared with radius twice as great, and density approximately four times lower than "SDREVC". Because N is reduced by cutting axially, the plasma radius r_p is roughly constant across a data series, and the density n is correspondingly lower for lower N points. Middle: Temperature diagnostic signals (black, overlaid) and single fit (red) for five plasmas. These plasmas were passively cooled to $T = 30\,\mathrm{K}$ and then evaporatively cooled to $T = 8\,\mathrm{K}$ with $N = 2 \times 10^6$ particles remaining. Right: Images of the evaporatively cooled plasma. Top image (fast dump) shows that the radius $r_p \approx 0.5\,\mathrm{mm}$ after evaporative cooling. Bottom image (slow dump) exhibits the usual 'cored' profile, i.e. most particles come out at low radius, which only occurs when the plasma is several Debye lengths thick radially.

account, see Ref. [102]).

A movable shield cannot be used to protect the positron plasma during antihydrogen beam formation. The shield must be open so that antiatoms can exit the trap. An alternative, suggested by Fritz Caspers, was to (1) add cryogenic microwave absorbing material to the trap and (2) permanently cover both axial extremities of the cryogenic trapping region with a fine copper mesh. The mesh chosen reduces microwave transmission at frequencies of interest by over 20 dB while maintaining 79% transparency to particles. This design was adopted for the final installation in the new cold bore. The results were dramatic and immediate. By the end of the first day using the new trap, cues which previously yielded plasma with $T \approx 120\,\mathrm{K}$ now yielded $T \approx 35\,\mathrm{K}$ with almost no modification.

The 2021 run was nearly over by the time the new trap was operational. This left less than two weeks for development prior to a series of water and power interruptions which required the apparatus to be shut down. Only electron plasma was tested, and only in one portion of the trap. The results obtained with electron plasma are nevertheless very promising (see Fig. 26). In particular, it seems that up to 40×10^6 particles can be passively cooled to $T < 30\,\mathrm{K}$. This is at least a factor of ten more particles than was reported for the ALPHA mixing scheme. That fact has immediate consequences for the foreseen ground state antihydrogen yield.

The number of antiprotons used in mixing is limited by two things. One is the number of antiprotons available. In this domain ASACUSA still holds the record for most antiprotons trapped, and remains the leader for trapping efficiency in the ELENA-era by a wide margin (see Section 5.1). The second limitation is the number of positrons, which serve as a thermal bath for the binding energy of the antihydrogen. With ten times more cold positrons, ASACUSA could conceivably maintain a cold positron plasma while mixing with ten times more antiprotons than before. That might increase the antihydrogen yield by yet another factor of ten relative to previous results.

7 Proton Source

In previous SPSC reports [98, 103] we described the functionality and the first tests of the proton source performed in Vienna. It was initially planned to transport the proton source for commissioning to CERN in January 2021, but this was delayed till June 2021 due to Covid-19.

After commissioning the source with the same setup as in Vienna [98], we spray-painted the bare copper electrodes with colloidal graphite and connected the assembly to the experiment at the position where MUSASHI is usually mounted. We added three magnets (Higaki A, B and C) to the transfer line between the source and the trap. These have the added benefit of increasing the magnetic field in the proton source (Fig. 27), which improves trapping.
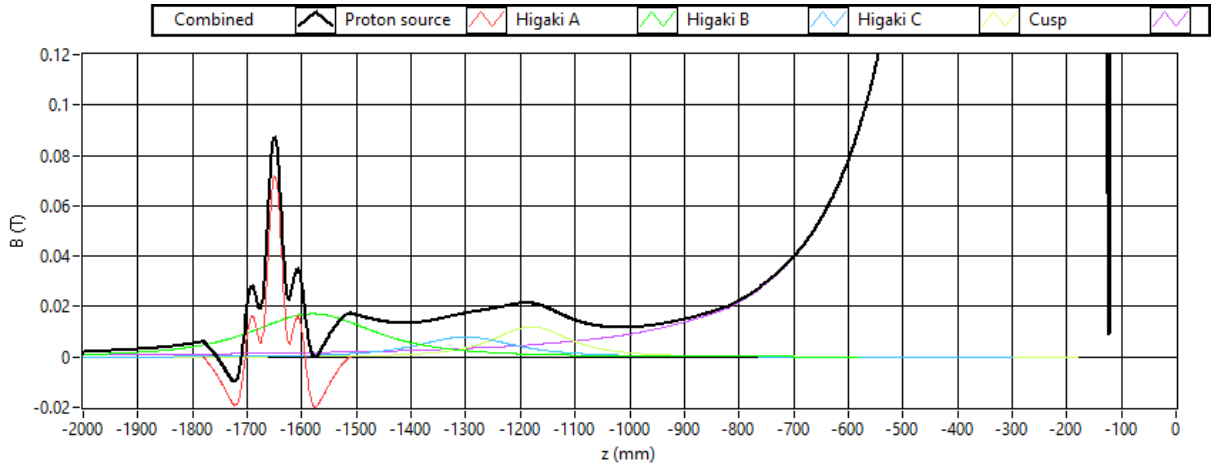

Figure 27 – On-axis magnetic field from the proton source to the Cusp trap, showing the fields from individual magnets and the total field.

Extrapolating from earlier results at low electron source current, we expected to produce up to 2×10^6 protons per second with the electron source at sufficiently high current. Such high currents and high repetition rates turned out to be incompatible with the pulsed delivery scheme implemented in 2021. In particular, the optimal repetition rate was found to be about 10 pulses s^{-1}, not 1000. It required about 30 s to accumulate 10^6 protons at this rate. To measure the number of trapped protons, we used the upstream plasma detector as a Faraday cup. We then biased the MCP-phosphor assembly and used a silicon photomultiplier (SiPM) to measure the light coming from the phosphor screen, calibrating the light yield to the amount of charge determined previously by the Faraday cup measurement. The number of protons and H_2^+ is shown in Fig. 28 as a function of catching cycles. Each cycle took about 100 ms. We accumulated approximately one million protons in about 30 s; for a higher number of catching cycles the detector is saturating. By specifying the number of catching cycles, we are able to control the number of protons in the trap. In Fig. 28 one can also see the result of a cut off curve measurement of the proton and H_2^+ beam produced, showing an energy spread for the protons and H_2^+ of 5.7 eV and 5.3 eV, respectively. This measurement was done by scanning the voltage of the last electrode of the source and measuring the protons and H_2^+ caught in the Cusp trap and extracted onto the MCP.

These measurements show that we can produce and catch a large number of protons in a relatively short time compared to antiprotons. This opens the possibility to refine our plasma handling, mixing, and de-excitation methods using matter-equivalent particles in periods during which CERN does not deliver antiprotons.
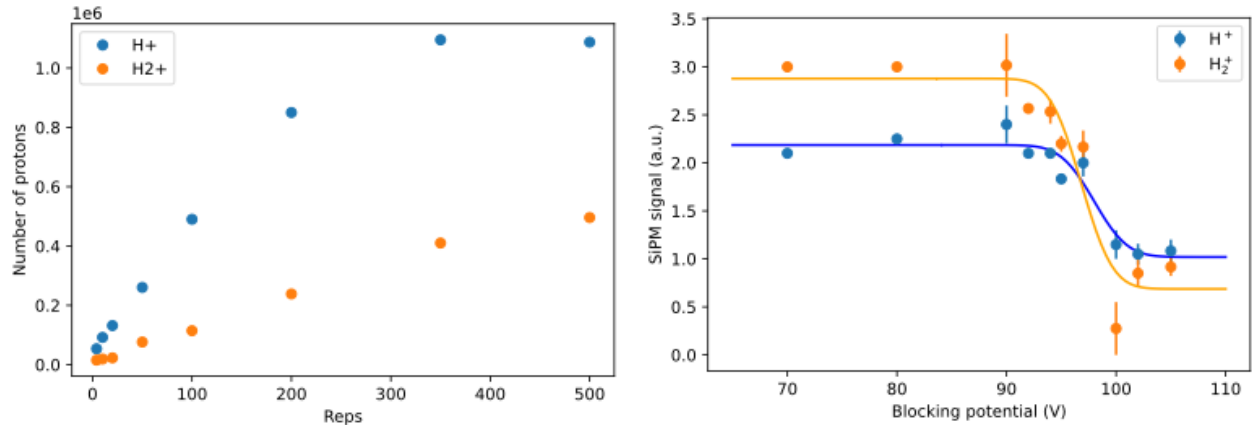
Figure 28 – Left: Number of protons and H_2^+ extracted from the Cusp trap as a function of catching cycles (Reps). The time needed to catch 500 times is about 55 s. For N$> 10^6$ the detector is saturating. Right: Energy spread of protons and H_2^+ blocked with the last electrode of the proton source. The data points are fitted with $f(x) = c + A \cdot \text{erf}(\frac{\mu - x}{\sqrt{2} \cdot \sigma})$ with $\sigma = 2.4$ and $\sigma = 2.3$ being the standard deviation for H^+ and H_2^+, respectively, which determines the energy spread.

8 Positrons

It was planned that during 2021, we would install the new room temperature, conventional conducting magnet, Surko type buffer gas trap (from the University of Aarhus and produced by First Point Scientific). Unfortunately, due to delays caused by Covid related travel restrictions, this was not possible thus, the existing trap was used again in 2021.

Due to the new location of the incoming beam from ELENA, the positron trap location was exchanged with the Cusp trap. Hence, we had to re-optimize the alignment, control routines and timings of the trap to reproduce the results of 2020 (approximately 2 million positrons in 30 s [98]). We were able to accumulate 1.3 million positrons in 30 s this year with little optimization, however as the new accumulator described below was expected to work with the FPS trap which has a higher repetition rate (shorter lifetime) work commenced on reproducing these conditions. With a higher buffer gas pressure ($1e^{-6} \rightarrow 4e^{-6}$ mbar) and optimization of the trapping potential, we were able to trap about 180 thousand positrons in 3 s.

8.1 Positron accumulator

Within the framework of the replacement of the positron trap, we developed, installed and carried out a test of functionality of a positron accumulator (from here on called *stacker*). The stacker is a multi-ring electrode Penning-Malmberg trap meant as a second-stage accumulator, cooler and buncher of positrons delivered by the Aarhus-FPS trap system at a rate around 0.5 Hz in order to match the duty cycle of the antiproton line and deliver cool positrons in a single macrobunch of 10^8 particles to the Cusp; the single-injection, two-stage system will decouple more efficiently the Cusp from the higher-pressure positron cooling stage [98, 103].

The stacker design was completed and orders for its parts (electrode stack and assembly items) were placed by the end of 2020. The original schedule foresaw the delivery of all components to Milan, Italy during Spring. This was made impossible by delays related to the pandemic emergency, as many manufacturing companies experienced a slowdown in production times. Concurrently, travel from Italy to CERN was halted up to July.
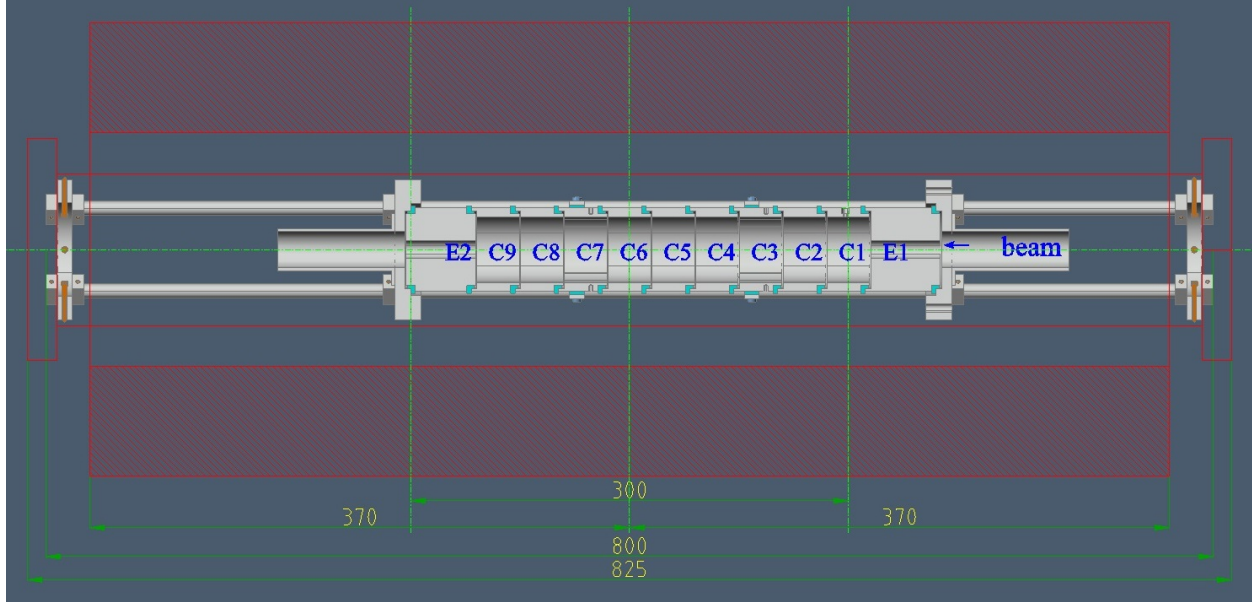
Figure 29 – Cross sectional drawing of the stacker electrode tower. Magnet and vacuum chamber are sketched in red for reference. All dimensions in millimeters.

Despite these setbacks, we managed to carry out the installation of the stacker within the time span of the 2021 beamtime. All of the electrode stack parts were delivered in early July at the Milan site, where all metal surfaces facing the positron beams were spray-painted with a conductive graphite coating. The assembly of the stack and the in-vacuum cabling started in August, as soon as all parts reached the AD. The full stack (see cross-sectional drawing in Fig. 29) comprises nine inner electrodes of equal size (C1 to C9, inner diameter 45 mm) and two trapping electrodes with an inner diameter 12 mm, enclosed between two assembly rings. The compact setup provides a number of advantages, such as flexibility in the shaping of the axial potential profile and a relatively closed environment, limiting the buffer gas conductance to the rest of the vacuum environment. Electrodes C3 and C7 are azimuthally split in four sectors as we envisage the opportunity to perform rotating-wall (RW) compression on both the hot component of the positron sample and the cool fraction being accumulated in a nested potential trap in the downstream half of the stack (see also [98] for further design details). The assembled stack (Fig. 30) was installed and mechanically aligned inside the first solenoid of the transfer line connecting the existing positron trap to the Cusp. The installation required the replacement of the vacuum vessel; the vacuum section from the exit gate valve of the positron trap (presently used as the first trapping and cooling stage) to the end of the transfer line was finally closed and pumped down in early October.

The transmission of electrical signals to and from electrodes can be affected by unwanted disturbances like impedance mismatches and noise. Technical measures implemented to reduce these issues include the use of 50 Ohm coaxial cables, double-ended coaxial multipin feedthroughs on the air-to-vacuum flange and lowpass filtering electronics placed right at the flange feedthroughs within a 10 mm thick Aluminium box acting as a noise shield. In addition to lowpass filters, the electronics boards mount reed relay switches for RF signals on trapping electrodes E1 and E2 as well as on C3 and C7 inner electrodes in order to apply synchronized confinement- and RW-compressing fields, respectively. The design of printed circuit boards follows the one already implemented in the Cusp trap, where it has proved effective in the suppression of high-frequency noise which would translate into plasma heating. The filter box and electronics boards were prepared in Milan and
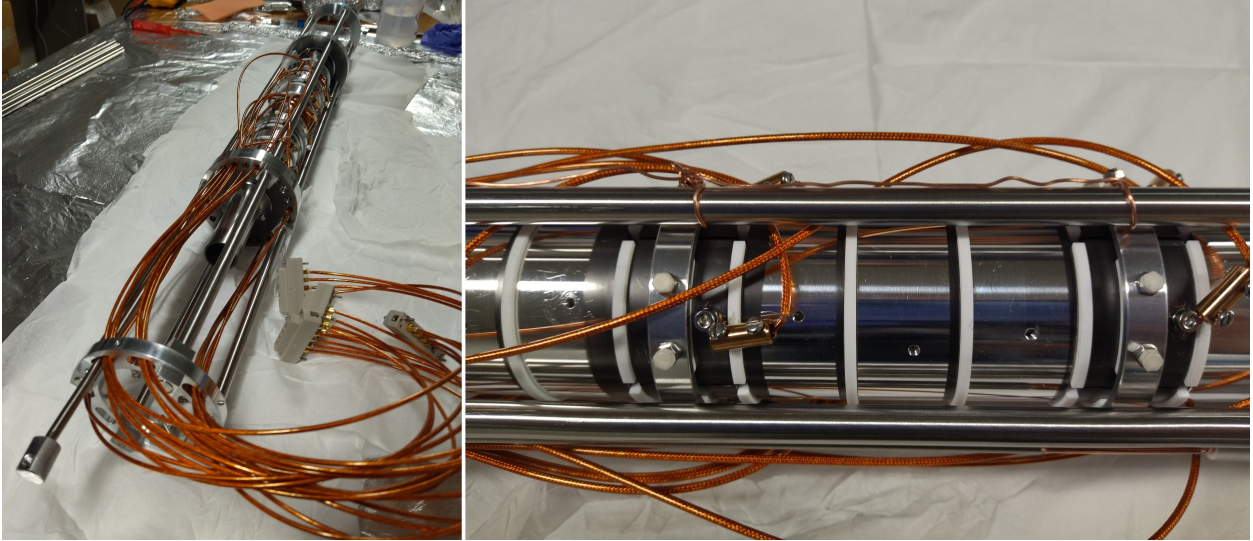
Figure 30 – Left: Full assembly of the stacker electrode tower with electrical connections. Right: Detail of the central part of the stack (C3 and C7 split electrodes are visible).

then installed in October.

Although a dedicated detector system downstream is not in place yet, after the optimization of the accumulator catching, cooling and release cycle we carried out a series of initial tests of operation of the stacker in November. To this aim we implemented a basic integration of the stacker handling into the general control system of the beamline, including the control of magnet current and electrode potentials. We could verify both beam transmission through the grounded stack and beam blocking on any stacker electrode, by setting a positive potential of some ten volts on the selected electrode. A preliminary bunch catching routine was set up; by ejecting the beam towards the upstream side and measuring the annihilation signal at the position of the first-stage positron trap exit gate valve, we could get a qualitative proof of beam trapping at a residual gas pressure in the low 10^{-7} mbar. A gas line for the SF_6 buffer gas was also connected and gas injection was tested, although it is not implemented in a trapping and cooling scheme yet.

We can conclude that the basic functions of the stacker are demonstrated. For the next year, a number of developments of the positron line are envisaged. The first priority is the transition from the current positron trap to the Aarhus-FPS trap. The new system, including the source and moderator unit and a multi-ring electrode trap, must be completely reassembled and recommissioned. Optimized positron bunches ejected from the FPS trap must then be accumulated in the stacker; to this aim we will perform a thorough campaign of tests to tune a trapping-compression-cooling routine of many stacked positron bunches. This will require a full characterization of trapping pulse amplifiers and the tuning of both potential timings and buffer gas pressure. The whole positron line control shall be definitively integrated into the general control system of the experiment. Opportunities for destructive and non-destructive (collective mode-based) detection of trapped and ejected plasma features will be evaluated. Hardware-wise, when the Aarhus-FPS machine replaces the current trap, a six-way cross piece will be installed upstream of the stacker and will allow us to redo all electrical and gas connections upstream, as per the original design (not implemented in the first installation due to space constraints). While this will not alter the functionality of the stacker, it will further reduce the gas load on the downstream line. A modification of the support frame allowing for height adjustment can also be considered.

9 Antihydrogen detector upgrade

9.1 Data Acquisition Hardware and Software Upgrades

Previous results showed that the antihydrogen formation rate is peaked at a few seconds after start of mixing. New mixing schemes developed focus on a mixing cycle of about one second duration. Expecting an increased production rate of antihydrogen, a higher readout speed of the detector is needed. As the average rate of cosmics is only of the order 1 Hz, this underground will be much less important and thus the time resolution requirement – previously a key parameter to distinguish cosmics from annihilation pions by their TOF through the detector – can be relaxed in favour of readout speed. The DAQ system previously developed by C. Sauerzopf [104] and M. Fleck [105] had to be changed to enable readout rates higher than 50 Hz. Instead of analogue signals and wave form digitisers now digital time-over-threshold signals from the hodoscope bars are recorded. This lead to replacing or adding hardware and reprogramming some of the software.

DAQ Hardware For trigger production two FPGA logic units are used and all the digitisers were replaced by a single 128 channel TDC. Two other TDC units are used for the detection of signals on the fibres. The VME crate additionally houses a VME controller (SIS3104) that connects it to a computer via optical link fibre.
On the CAEN V2495 general purpose logic units the LVDS inputs are used for the creation of coincidence signals as trigger. It is then distributed to each TDC and the SIS. Without alterations, the hodoscope bar signals are put out in the lower connectors of the logic modules and then transferred to a TDC.
The CAEN V1190 TDCs are used in trigger matching mode. This means that after receiving the trigger, a programmable time window is searched for signals. It can detect either individual leading and/or trailing edges or a leading edge with its corresponding pulse width. For the new setup the edge detection was changed to leading and trailing edge instead of pair mode (leading edge and pulse width). This was needed because the signals of the hodoscope bars get inverted by the FPGA. Re-inverting the outputs would put a clock-jitter onto these signals. Instead, what the TDC sees as a trailing edge is handled like a leading edge in the analysis and vice-versa.

DAQ Software The MIDAS (Maximum Integrated Data Acquisition System) is a DAQ system developed at the PSI and TRIUMF [106], which has been successfully used in our experiment before, has been updated to the latest stable version (May, 2019).

New Polling Frontend For the new DAQ the MIDAS frontend was changed to accomodate the additional VME module as well as the omitted ones.
Inside the frontend also the EQUIPMENT needs to be defined. This is a structure that describes the event trigger type, for which the EQ_POLLED flag was chosen instead of the previous interrupting mode. This means that in a defined poll time (here 10 ms) the routine will be called as often as possible. A polling function checks whether a variable is true (for us `v1190_DataReady(vme, v1190Adr[0])`) before starting the readout routine `read_tdc_event`.
Switching to the polled readout allowed to readout events at ≈ 300 Hz without loss, see Fig. 31.

TDC in Block Transfer Mode To improve the possible count rate further the BLT (block transfer) mode of the TDCs is used. A previously defined number of events can be transferred at the same time, meaning the system waits until that number is reached before the transfer starts.
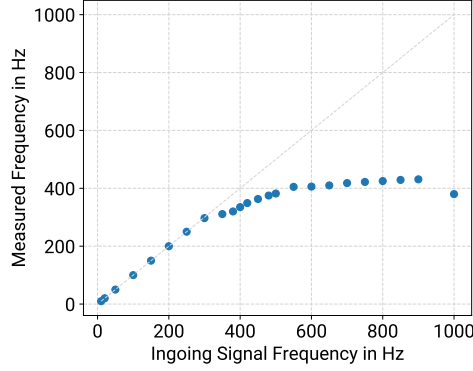
Figure 31 – After changing to polling mode the measured signal rate was compared to the real frequency of a signal produced using a waveform generator.

This enables faster readout since the time-consuming process of data transfer is done less frequently. For example in the single event mode the readout takes $\approx 0.5\,\mathrm{ms}$ per event while in BLT mode one event is read in $\approx 10\,\mathrm{\mu s}$.

Using the new frontend together with the BLT mode it was possible to detect events at a rate of over $1\,\mathrm{kHz}$. Compared with the previous data acqustion, this represents an improvement of a factor 100.

Event Trigger Upgrade   Until the last beam time in 2018 a trigger system using several NIM logic modules was applied together with an FPGA VME unit. A coincidence signal was produced when there was a signal for both the upstream and downstream silicon photomultiplier (SiPM) of at least one outer bar and one inner bar. This coincidence signal was then further processed and the final trigger was produced when signals from the FPGA and the central BGO crystal scintillator were present.

For the new setup two CAEN V2495 "Programmable Logic Units PLUS" [107] were used. Due to limited connector space the readout had to be split up into the two logic units.

Inside the FPGA logic coincidences between the upstream and downstream ends of a bar are made to avoid triggering on dark noise of a single SiPM. If there is at least one signal on one outer bar and one inner bar, a logic impulse is produced inside the FPGA unit. Since only half of the bars are connected to one unit, this coincidence signal of FPGA1 is transferred to FPGA0 via a LEMO 00 connection. Inside FPGA0 they are linked with an or-condition to create the final coincidence trigger.

Besides a $1\,\mathrm{ms}$ self veto, a veto signal is also sent from the SIS 3104 VME to VME link for the duration of the readout and during antiproton injection a veto signal is sent from the AD. The final vetoed trigger signal is distributed to the 3 TDC units and the SIS 3104 module. The whole trigger logic can be seen in Fig. 32.

Raw Data Analysis   To pre-analyse the recorded raw data, the MIDAS files are converted to ROOT files by the `analyser` programme previously developed by C. Sauerzopf [104] and modified by M. Fleck [105]. To accommodate our modifications, several changes were implemented.

The `analyser` programme is composed of several files where each one has its own task. The MIDAS file is read in a file that sends the data event by event to another one which transfers it word by word to be divided into the appropriate ROOT leaves. The ROOT trees and leaves are defined by other programs.
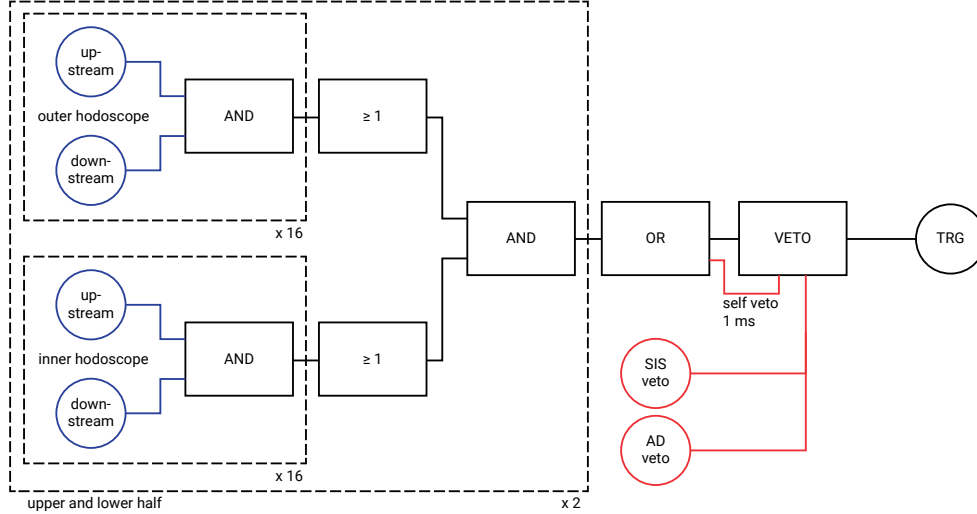
Figure 32 – Upgraded trigger flow diagram, now fully programmed inside two VME FPGA units.

With the digitisers in use, the recorded signals were analysed using the `waveformlibrary`, a software library written by C. Sauerzopf [104,108]. Since no ADCs are in use anymore, this part was omitted from the programme.

Before the upgrade to BLT mode, the data transfer from the TDCs was also done event by event, meaning that each readout cycle corresponded to one event. For the block transfer a new system was implemented in order to reset the event number after each trigger signal and not each readout.

9.2 Testing the Hodoscope Time Resolution

In the new setup only digital time-over-threshold signals are used which are produced by leading edge discrimination. This introduces a jitter depending on the rise time of the signals. Due to the difference in rise times, the ToT signal is not produced at a certain fraction of the amplitude. If the signals are produced with SiPMs operated in saturation, the amplitude of all signals is maximal ($\approx 800\,\mathrm{mV}$). When taking the leading edge (LE) times at a specific threshold voltage, the signals are more constant due to the minimal rise times.

A measurement with a collimated ^{90}Sr source was performed at 5 different positions along bar 0 of the outer hodoscope. The time differences of the upstream and downstream leading edges are taken and the standard deviations lie between $1.25\,\mathrm{ns}$ and $1.79\,\mathrm{ns}$. These relatively large values are due to the SiPMs not being operated in saturation as this is not possible with the used amplifier boards. This was confirmed by a test conducted using two IFES (intelligent frontend electronics for SiPMs) amplifier boards [109] with different signal amplification factors on the same scintillator bar and the source placed on top of it. The normalised histograms of the leading edge time differences of downstream and upstream signals are shown in Fig. 33 together with their Gaussian fits. For the original amplifier board the standard deviation is larger than for the board with the higher amplification by a factor of ≈ 3. As a consequence of this measurement plans were made to increase the amplification on all of the IFES boards.
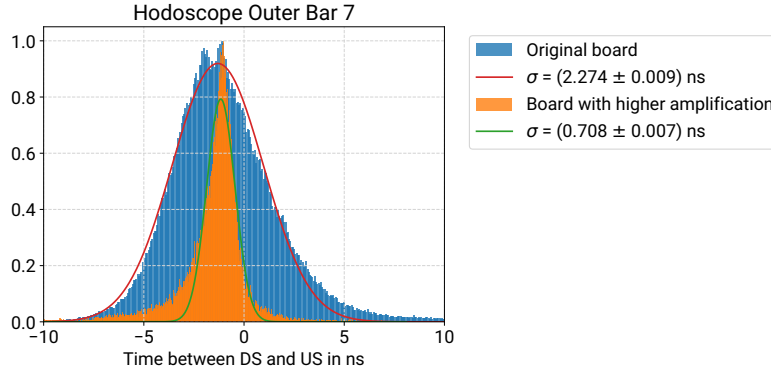
Figure 33 – Normalised histograms of the time differences between downstream and upstream leading edges. The blue distribution shows the data recorded for the original amplifier board and the orange data was detected using a board with higher amplifications and therefore SiPMs nearly in saturation. For both a Gaussian fit was performed where the standard deviations σ are printed on the right.

10 Study of annihilations with slow extracted antiprotons

The ASACUSA apparatus is also ideally suited for systematic studies of antiproton annihilation at rest, owing to the capability of the antiproton capture trap (MUSASHI) to provide extremely low-energy, quasi-continuous (DC-like) $\overline{\text{p}}$ beams [92]. The absence of degraders to moderate the $\overline{\text{p}}$ energy is advantageous because it suppresses pion contamination from upstream beam annihilations observed in similar measurements [110–112], and allows for annihilation prongs to be measured with almost zero background. The very low energy of the antiprotons also allows the use of very thin targets, thus removing the stopping effects and production of secondaries and enabling the detection of the heavy nuclei produced in the annihilation process.

As described in [113] and [98], we have performed antiproton-nucleus ($\overline{\text{p}}$A) fragmentation measurements using very low-energy antiprotons (<1 keV) and targets of 1–2 μm thickness in order to validate the different descriptions of the $\overline{\text{p}}$ annihilation at rest in the Geant4 models [114, 115] and FLUKA [116]. The preliminary results suggest that, while the Geant4 models show somewhat good description of the measured data for the pion multiplicity [98], the production rate of nuclear fragments is severely underestimated, being off by a factor 2–16. The distributions for the multiplicity of heavily ionizing particles for $\overline{\text{p}}$ annihilation in carbon and gold, recorded with Timepix3 [117] are compared with data in Fig. 34. The results from these measurements will be published together with FLUKA simulations, which are currently being finalized.

10.1 Systematic study on antiproton-nucleus annihilation at rest

Production of antihydrogen and its detection through annihilation are the basis of most of the experiments at the AD [118–122], which makes the antiproton-nucleus ($\overline{\text{p}}$A) annihilation at rest the main process of interest for efficient detection and correct tagging of antihydrogen.. Our previous studies, but also others at the AD, ascertain that the measured data are not well reproduced by the available Monte Carlo models, which indicates that the mechanism of the antiproton-nucleus annihilation at rest is still not well understood. Moreover, the scarce amount of data make any attempt for tuning of the simulations impossible. Our discussions with the Geant4 group at CERN, on the lack of a reliable simulation code for antiproton annihilation at rest, led to the conclusion that developments for better simulation of the secondary fragments production require experimental data on a wide range of nuclei, as they can undergo different types of hadronization depending on
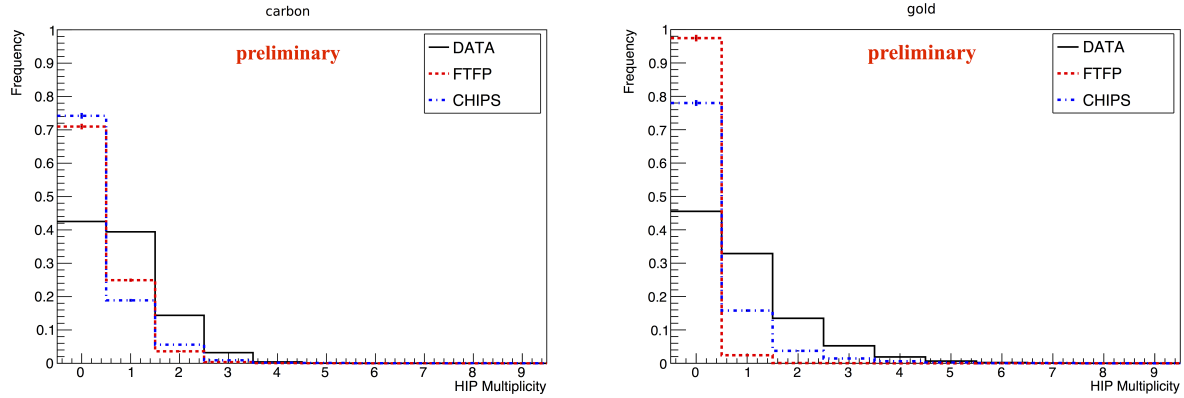
Figure 34 – Multiplicity of heavily ionizing particles recorded by the Timepix3 detector, compared to Geant4 models, for $\overline{p}$ annihilation in carbon and in gold.

their mass and excitation energy [123]. We have thus proposed, as part of the ASACUSA program in the ELENA era, to build a parasitic beam line for measurements with slow extracted low-energy antiprotons [124] which do not interfere with the $\overline{H}$ experiment.

In 2021 we were granted funding by the Austrian Science Fund (FWF, project number P 34438) to measure $\overline{p}A$ annihilation in $\sim 4\pi$ sr for a complete and representative set of light, medium-heavy and heavy nuclei to validate the existing models, and to also explore some of the $\overline{p}A$ process unknown traits, such as the Final State Interactions (FSI). We have established a collaboration with a group at CEA, France, which is aiming to extend the available Intranuclear Cascade of Liège (INCL) code [125] on $\overline{p}A$ interactions. The results from our measurements will be exploited to directly validate their new calculations, specifically developed for $\overline{p}A$ reactions.

The project started in mid-2021. The two milestones for 2022 are (i) the design and installation of a dedicated beam line for $\overline{p}$ slow extraction in ASACUSA and (ii) the design and construction of the target and of the 4π detector.
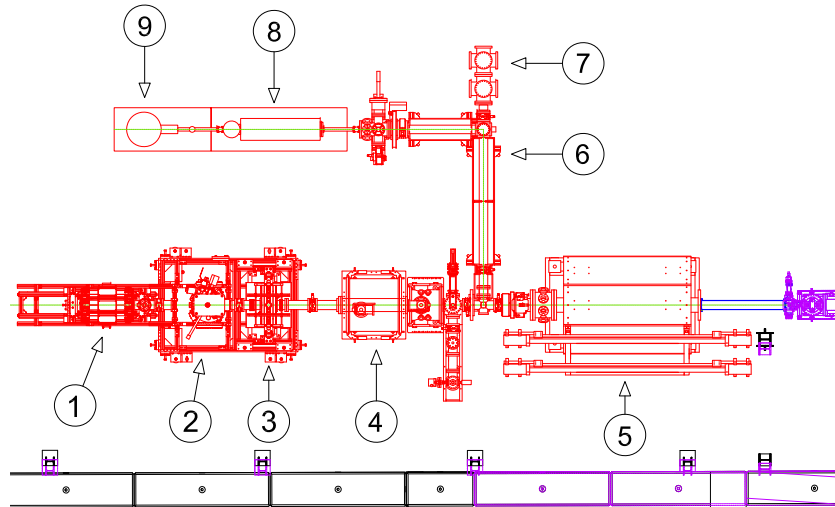

Figure 35 – Sketch of the various parts of the ASACUSA apparatus.The $\overline{p}$ enter from the left. 1) Hodoscope, 2) Sextupole, 3) Microwave cavity, 4) Cusp trap, 5) MUSASHI trap, 6) e$^+$/$\overline{p}$ transfer line, 7) Slow extraction set-up, 8) e$^+$ accumulator, 9) ^{22}Na source.

As mentioned before, MUSASHI has the ability to routinely work in two operation modes for p̄ extraction: pulse extraction mode providing pulsed beams, which is used for the H̄ experiment, and DC extraction mode for long bunched beams, which will be used for these annihilation studies.
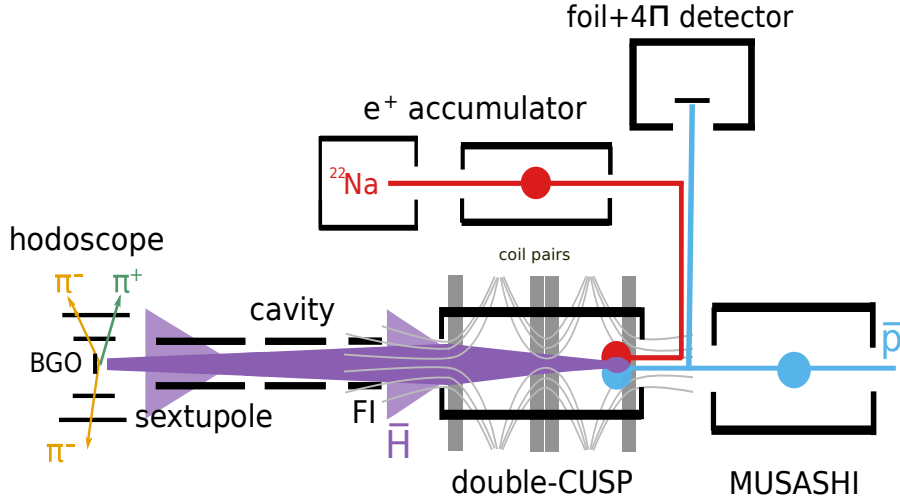

Figure 36 – Sketch showing the particle trajectories of the two experiments operating at the ASACUSA facility.

The slow extracted antiprotons from MUSASHI will be transported to the annihilation target through the positron transfer line (number 6 in figure 35), stretching between the e^+ accumulator and the Cusp trap. The p̄s will be transported by an electrostatic quadrupole deflector [126] to be installed in the six-way cross that connects MUSASHI and the e^+ transfer line. The geometrical configuration of the quadrupole and of other beam optics elements such as Einzel lens is being explored with the SIMION simulation package [127]. We aim to finish the design in early 2022 and to manufacture the required parts in the first half of the year. The goal in 2022 is to demonstrate the efficient transport of antiprotons to the annihilation target. Simulation work for the design of the detection chamber (number 7 in Fig. 35), which will host the annihilation target, will take place in parallel.

Following the successful implementation of the Timepix3 ASIC coupled to a thick silicon sensor, the same detector, or its successor, Timepix4 will be further used for this study. The foreseen configuration is a 3D stacking in a cube-like formation, where five faces host Timepix3 quad detectors, while the side of the incoming beam consists of four individual Timepix3 ASICs, with spaces between them to allow for the beam to reach the target.

Once the conditions for efficient p̄ transport are established, an estimate of the required beam time is ∼250 hours for a systematic study of 15 different nuclei and 4 isotopes (∼50 hours of beam time were previously consumed for data taking with 3 target elements). With the round-the-clock operation of ELENA and the increased number of antiprotons with keV energies delivered to the experiments, about half a day (12 hours) of beam time per target should be sufficient. Additional time will be required for changing the target foils. As this experiment shares the e^+ transfer line with the H̄ experiment, vacuum of $\sim 10^{-9}$ mbar will have to be achieved before opening the gate valve between the slow extraction set-up and the e^+ line, meaning that 1–2 days will be consumed for pumping and bake-out when changing the target. Thanks to the 24 hours operation mode of ELENA these measurements will be performed in 2023 and 2024 without significantly disturbing the H̄ experiment.

11 Plans for 2022

Fig. 37 shows an ideal timeline for the work in 2022. Before antiprotons are available there are a number of maintenance/installation tasks which we will perform including reconditioning the Sextupole magnet and installing the First Point Scientific style trap which was delayed from 2021 to 2022 [98]. During this period and continuing during beam time, offline experiments will be performed on plasma in the Cusp, accumulation of positrons, and measurements of the residual magnetic field in the microwave cavity to allow the construction of compensation coils (see section 11.1.2).
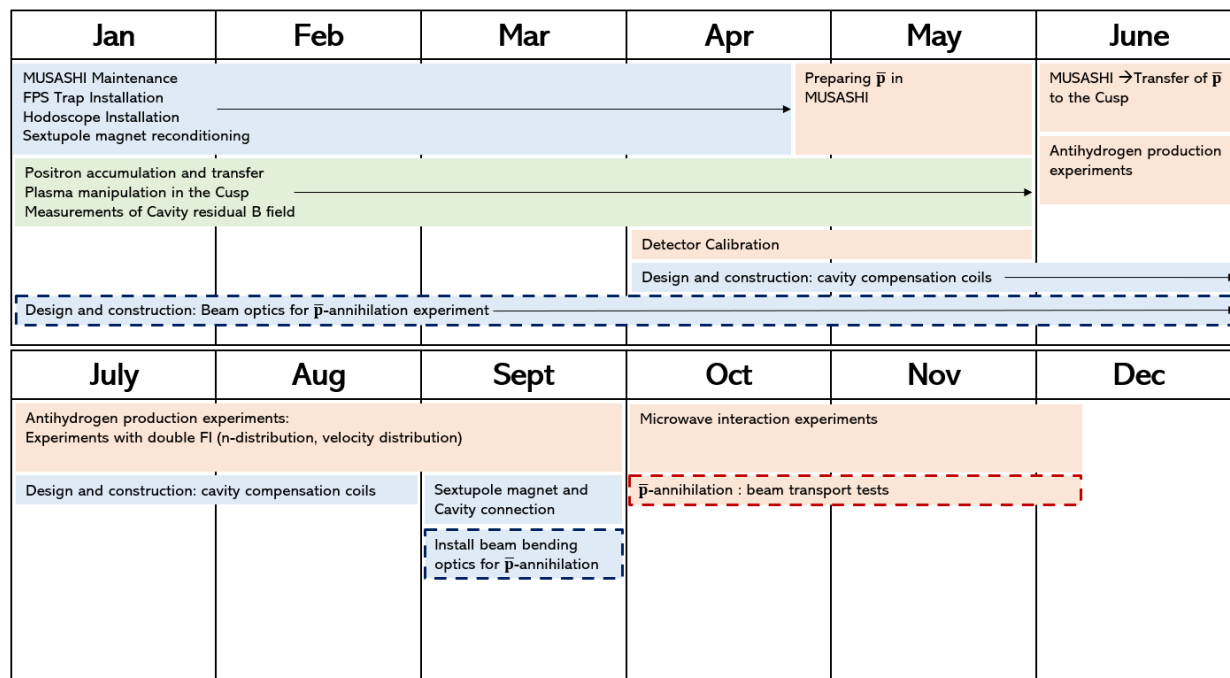
Figure 37 – Chart shows schedule for 2022. Colour key– blue: work with hardware, green: offline experiments, orange: beam time. Dashed outline show entries for the antiproton annihilation experiment.

Once antiprotons are available, MUSASHI will be commissioned and then work on transferring antiprotons to the new Cusp trap will commence. As soon as antiprotons and positrons are available in the Cusp trap, we will begin a systematic study of the antihydrogen production process in the new Cusp trap. If all is successful, then later in the year we will install the microwave cavity and focusing sextupole magnet between the Cusp and hodoscope antihydrogen detector and attempt to observe antihydrogen interacting with microwaves in the cavity.

The antiproton-annihilation experiment will commission the beam bending optics during periods of downtime for the antihydrogen experiment (see section 10).

Part III
Experiments with hydrogen beams

In this section we give a brief summary of the progress with ASACUSA's parallel matter beam experiments in 2021 and on the plans for 2022. The developments and experiments with hydrogen consists of three main activities: precise and comprehensive characterization of the spectroscopy apparatus for the application to antihydrogen spectroscopy in a beam (11.1.1), hydrogen hyperfine spectroscopy for tests of Lorentz invariance in the context of the Standard Model Extension (SME) (11.1.2), and tests of fast stimulated deexcitation techniques in view of implementation in the antihydrogen experiment (11.2). The first two activities are performed on a complete Rabi experiment beamline (11.1), while a second dedicated hydrogen beamline has been constructed in 2021 in a new laser room built purposely for the deexcitation activities.

11.1 Progress at the hydrogen HFS-experiment

The hydrogen beam set-up is a complete Rabi experiment, where the spectroscopy components and methods for $\overline{\mathrm{H}}$ can be tested. In Fig. 38 a sketch illustrates the essential components above a photograph showing the current status. Details of the different components of this beamline have been provided in previous reports.
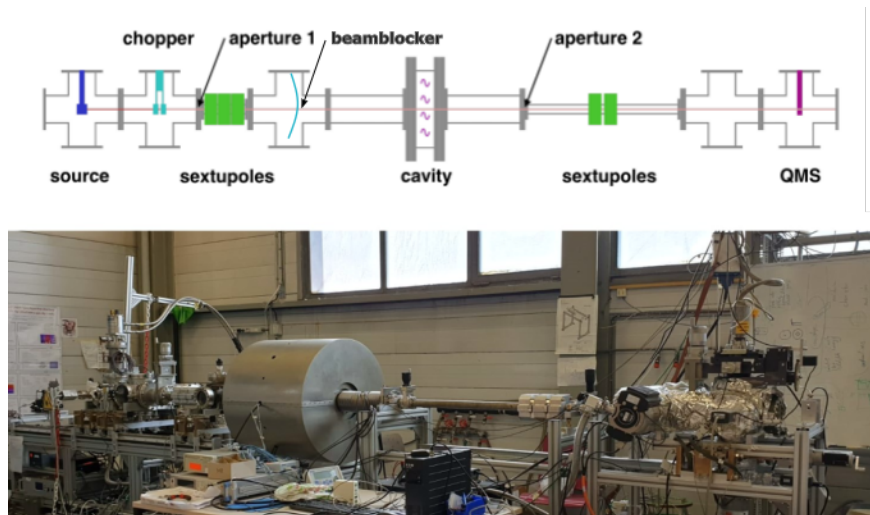
Figure 38 – Sketch and photograph of the hydrogen beam set-up. The atomic beam is formed on the left and gets modulated by a chopper and polarized by a set of permanent sextupole magnets. A beamblocker can be used to investigate the spatial distribution of the beam before it enters the interaction region consisting of a stripline cavity, field coils and a surrounding magnetic shielding. Subsequently another set of permanent sextupole magnets analyses the spin states before the beam is detected using a quadrupole mass spectrometer.

Following several maintenance and upgrade works performed on the apparatus in 2020, further improvements were done to the hydrogen source and supply line in early 2021 to counteract issues with contamination and leaks leading to decreasing hydrogen beam rates with time. Those issues have to date not been entirely solved and the continued operation of the beamline over several weeks remains difficult. However significant improvements were observed which allowed to perform three data-taking campaigns for SME tests and complete the foreseen measurements for the

characterization of the $\overline{\text{H}}$ apparatus.

11.1.1 Characterization of the $\overline{\text{H}}$ spectroscopy apparatus

Since its installation at CERN the hydrogen beam set-up has been used successfully to characterise spectroscopy equipment for ASACUSA's $\overline{\text{H}}$ experiments, namely the spin-state analyzing super-conducting sextupole, the cavity-assembly for σ transitions only, and the second cavity-assembly for σ and π transitions [128, 129]. When drawing conclusions from the observations with H to $\overline{\text{H}}$ it is important to factor in differences and uncertainties of the beam properties. While the velocity could be tailored to match the anticipated value for $\overline{\text{H}}$ the profile of the H beam is clearly smaller. Both beams are of annular shape as the central beam component is blocked for being weakly po-larised. However, while the outer diameter of the $\overline{\text{H}}$ beam can be as large as 100 mm the H beam diameter amounts only to 40 mm. In order to get a handle on this remaining uncertainty the cavity-assembly for σ and π transitions was mounted on a stage (compare Fig. 39 left) allowing to move it in transverse directions to the beam. In addition a helical beam blocker (compare Fig. 39 right) is installed upstream and by rotating it through the beam two-dimensional information on the den-sity distribution within the annular beam shape can be reconstructed. These measurements have been performed at the end of summer 2021 and provided an interesting insight into the size and origins of field deviations. The data has been taken and analysed in the course of the internship of Sebastian Lahs. Results from this preliminary analysis are presented below. Especially a critical investigation on systematic uncertainties is not included at the present stage.
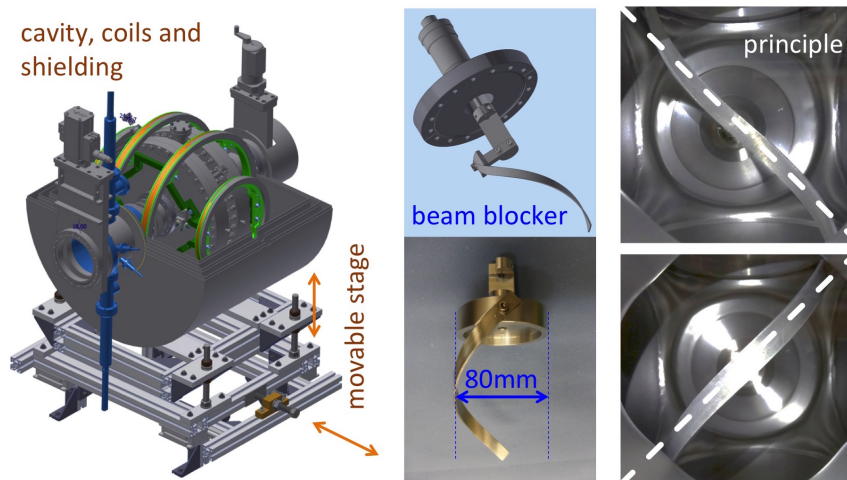
Figure 39 – Left: cavity with McKeehan-like coils and 3-layer cylindrical magnetic shielding mounted on a stage for displacements transverse to the atomic beam direction. Right: rendered image and pho-tographs of the helical beam blocker to illustrate working principle for two-dimensional beam profiling.

The assembly has been displaced in eight directions from the center position. For the vertical and horizontal displacements the assembly has been moved by 30 mm either up, down, to the left, or to the right. The other four directions correspond to diagonal displacements, whereby the assembly has been moved both vertically and horizontally by 20 mm, resulting in a displacement from the center of 28 mm. An overview on the probed volumes is shown in Fig. 40 top left.

Sets of transition measurements have been performed at those eight displaced positions and three times at the center for reference. Sets consisted of either four or six pairs of σ and π transitions, depending on the available measurement time, i.e. over night more extensive sets have
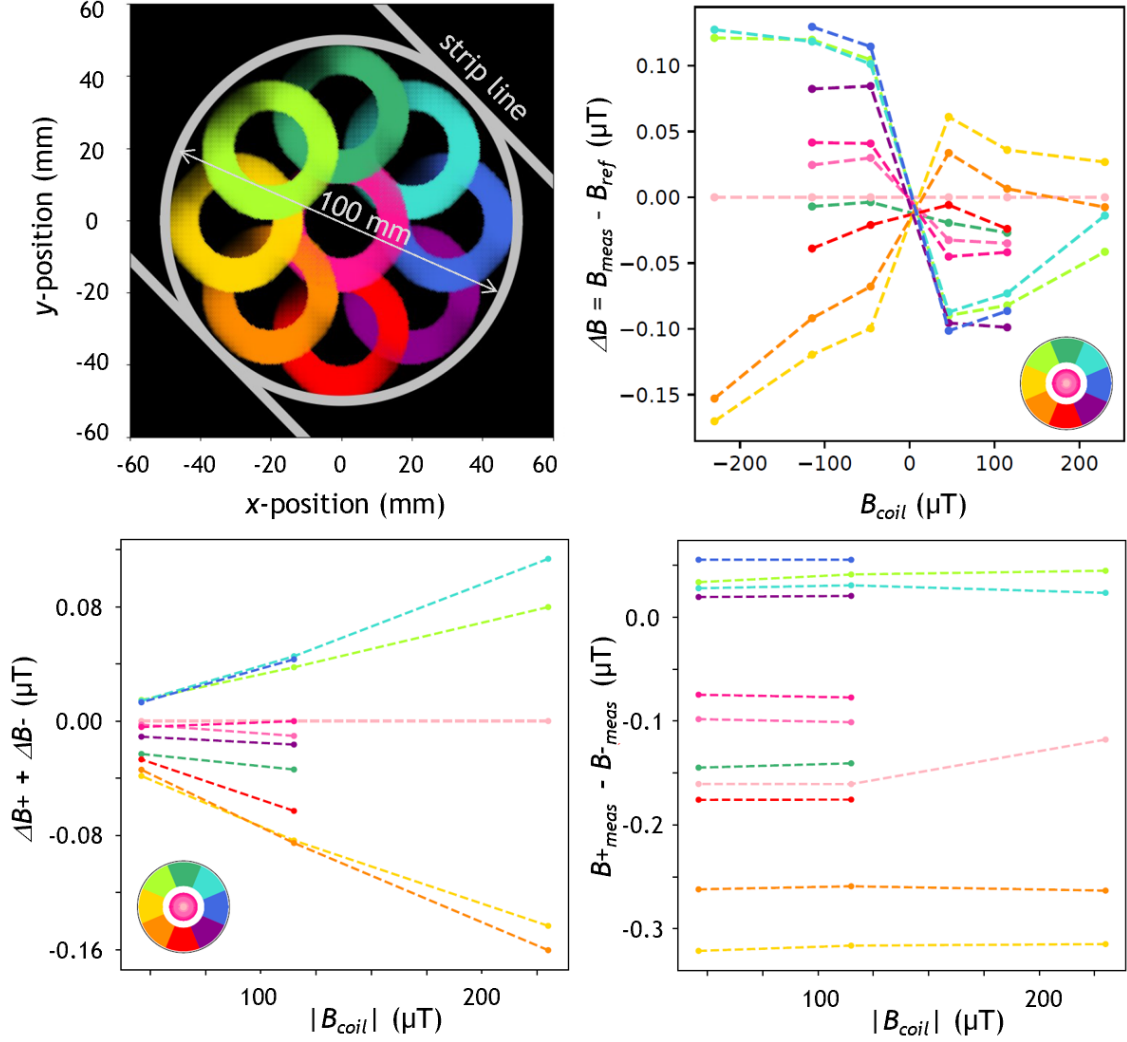
Figure 40 – Top left: Illustration of the volumes probed inside the strip-line cavity during the measurements at differently displaced cavity. Projection as seen in beam direction. The intensity of the color indicates the beam density as reconstructed from the scans with the helical beam blocker. The field produced by the coils points along the x-axis. The oscillating magnetic field is orientated at 45° parallel to the strip lines. Top right: Field deviations relative to a central reference for all measurements plotted against the coils' current expressed as the corresponding magnetic field. Bottom: Separation of the current dependent deviations of the coils' field and the current independent deviation caused by a background field. More details in the main text. Images are taken from the internship report of Sebastian Lahs.

been acquired. Every set used current values for the McKeehan-like coils of -0.5 A, -0.2 A, 0.2 A, and 0.5 A, while the larger sets include in addition the values of -1.0 A and 1.0 A. The corresponding values of the produced field are $B_{coil} \approx \pm 231\,\mu\text{T}$, $\pm 116\,\mu\text{T}$, and $\pm 46\mu\text{T}$. The obtained transition frequencies can be used to calculate the effective static magnetic field B_{meas} in the interaction volume very precisely. Due to the redundant information from two transitions this can be done in different ways. Independent of the chosen method the resulting overall picture is always the same and summarized by the plots in Fig. 40. Note, that the magnetic field changes by approximately proportional factors, when the current on the McKeehan-like coils is changed. In order to see the

position X , Y (mm)	set size Nr. of σ-π-pairs	ΔB_{coils} (nT/A)	ΔB_{bg} (nT)
0 , 0	6	0	0
-30 , 0	6	-168	-171
0 , -30	4	-129	-15
20 , -20	4	-45	181
-20 , -20	6	-168	-115
0 , 0	4	-17	62
30 , 0	4	76	216
-20 , 20	6	76	186
0 , 30	4	-92	18
20 , 20	6	92	174
0 , 0	4	-10	85

Table 1 – Summary of the extracted field deviations referenced to the first central measurement and separated into the field produced by the coils and the background field. The sequence of the rows represents the chronological order of the measurements.

small differences when comparing the fields of the same coils' current at different displacements of the cavity-assembly they are plotted relative to a reference measurement. Only one of the three sets acquired at the central position consists of six pairs of transition, therefore this set is chosen as reference. The resulting field deviations ΔB are plotted against the coils' current (given as the corresponding field value B_{coil}) in the plot on the top left of Fig. 40. The interpretation of this data becomes clearer, when realizing that the observed field deviations ΔB can have two contributions: One from the inhomogeneity of the field produced by the McKeehan-like coils and one from an inhomogeneous background field, which is not actively changed during the measurements. Considering that those two fields add vectorially and that the contribution from the coils' field scales linear with the applied current, one can see that the two contributions can be separated by building the sum and difference values of the calculated field deviations ΔB for the coils' current of identical absolute value but opposite sign. In the graph on the bottom left of Fig. 40 the sum value reveals the expected linear dependence of the field deviations on the field produced by the coils. And on the bottom right of Fig. 40 the difference values are shown, which should contain information on the background field as supported by the independence on the field produced by the coils. Note, that the earlier introduced reference can be omitted when looking at the differences, removing the arbitrariness of the chosen reference for the latter plot.

An overview of the extracted field deviations for all sets is given in Tab. 1. A quantitative interpretation suggests, that the larger fraction of the deviations stems from the background field. The largest field gradient from the center is observed towards the yellow data set and amounts to $7\,\mathrm{nT/mm}$. When scaling this as a worst-case scenario to the full diameter ($100\,\mathrm{mm}$) one obtains potential field differences of $0.7\,\mu\mathrm{T}$, which translate to frequency shifts close to $1\,\mathrm{kHz}$ for the π transition (the effect on the σ transition is much less and scales with the absolute value of the B-field). While this might sound like a limiting factor it is in case not for several reasons. First of all $1\,\mathrm{kHz}$ is still about a factor 10 smaller than resonance line width, meaning that the line profile only gets broadened and not washed out. Furthermore, when calculating the zero-field value of the HFS from a transition pair (σ and π), the leading error results from the σ transition measurement. Finally, this measurement only says something about the background field at the hydrogen experiment located in Bat. 275. Dedicated field measurements at the AD to design compensation coils to further reduce the fringe field of the Cusp magnet are already planned. The

unexpectedly large background field found here is a reminder that this step has to be done carefully. In fact the large value could be a hint that despite all care some magnetic material is present within the shielding. Magnetic tests on all materials will be redone early 2022 as well.

The field produced by the McKeehan-like coils proofed sufficiently homogeneous for the anticipated precision goal of the Rabi experiments on $\overline{\text{H}}$. Only at roughly 1.5 A the deviations will be of the same order as those of the background field. First measurements will happen at lower values, however, not too low in order to avoid effects from resonance interference. A good choice will be around 0.1 A corresponding to $23\,\mu\text{T}$, where deviations will be an order of magnitude lower than discussed for the background field above.

As a side effect this measurement also helped to understand an effect observed frequently in previous measurements with H, namely that the line shapes of the π resonances at the same absolute static field value but of opposite polarity can be different. The superposition of the two independent contributions to the field can posses a higher or lower uniformity than the individual fields.

11.1.2 Hydrogen SME-experiment with swapping B-fields

The cavity installed in the hydrogen beamline is capable of accessing the σ and π transitions due to a 45° alignment between the static and oscillating magnetic fields. Having access to the π transition is advantageous from a practical and theoretical point of view. From a measurement of a single pair of a σ and π transition the zero-field HFS can be calculated. This approach is sensitive to SME coefficients unlike a zero-field extrapolation of many σ transitions obtained at various static fields [130] or taking the difference of the π_1 and π_2 transition [131]. Furthermore, acquisition of only two transitions is sufficient, which reduces the beamtime requirements. Therefore, the present cavity-assembly is going to be used for ASACUSA's Rabi-type $\overline{\text{H}}$ spectroscopy as soon as sufficient rates of ground-state $\overline{\text{H}}$ have been observed. Given the short available $\overline{\text{H}}$ beamtime in 2021, the apparatus was used with hydrogen to constrain SME coefficients and gain more experience with the experimental and analysis methods using both transitions. Beyond the hardware improvements on the hydrogen source mentioned above, several hardware, slow control and software developments were carried out in 2021 to improve the quality of the data taken. Following those, three data-taking campaigns were realized in May, September and November 2021. In those measurements π and σ transitions are repeatedly measured sequentially and at opposite magnetic field orientations. The σ transition, which is insensitive to SME, is used as a proxy for the amplitude of the magnetic field, allowing to constraint the variation of the π transition with opposition orientations of the static magnetic field, a measurement which is sensitive to yet unconstrained SME coefficients. Due to the second order dependence of the σ transition on the magnetic field, the main limitation on the precision of the measurements is coming from the uncertainty on the magnetic field amplitude extracted from the σ transition. This limits the precision to a few hundreds of Hz (while the transition frequencies can be determined more than an order of magnitude more precisely), depending on the absolute value of the magnetic field at which the measurements are performed. However the main advantage of this technique is that the measurement of the magnetic field is done in-situ at the position where the transition is driven (owing to the similar trajectory of the two low-field-seeking states, which correspond to the initial states of the σ and π transitions in the cavity) limiting systematic effects. The analysis of the data is ongoing. A preliminary result on a partial data set is shown in Fig. 41. While this figure shows that the measurements of the π transitions at opposite magnetic field orientations are consistent within error bars, systematic effects leading to a consistently lower frequency measured than expected from the σ transition is observed and is under investigation.

Additionally, the hydrogen beam rates highly correlates with the goodness of the lineshape fit.

The main hypothesis for this effect is the difference of the cavity volume probed when part of the incoming hydrogen beam is clogged due to impurities in the source (the beamblocker located upstream of cavity enables probing the incoming beam spatial distribution). This hypothesis corroborates the results highlighted in 11.1.1 but needs further quantitative investigations. Those will provide a better knowledge on the lineshape which is highly relevant for the main $\overline{\text{H}}$ spectroscopy goal.
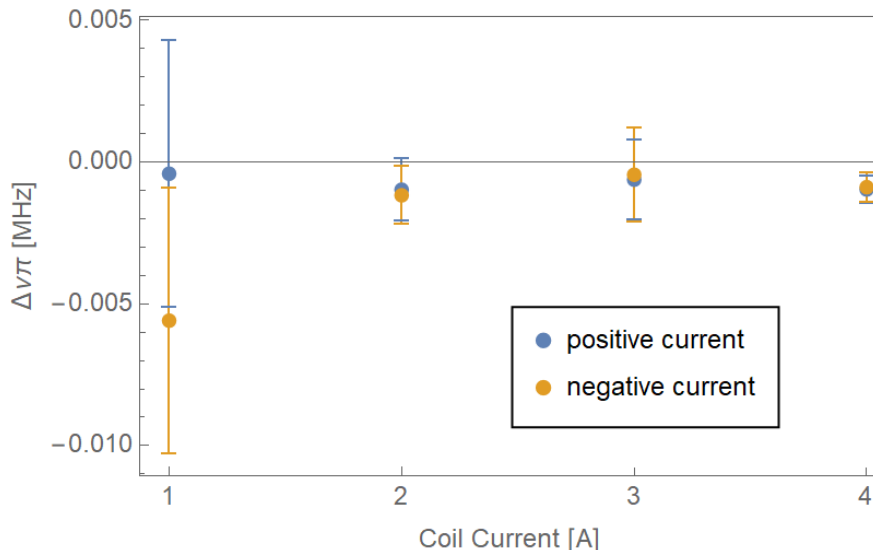

Figure 41 – Preliminary results from a partial set of data. $\Delta\nu\pi = \nu_{\pi\,\text{data}} - \nu_{\pi\,\text{exp}}$ is the difference between the frequency of the π transition measured ($\nu_{\pi\,\text{data}}$) and the expected $\nu_{\pi\,\text{exp}}$ value (calculated via ν_σ). $\Delta\nu\pi$ is plotted for both directions and different magnitude of the magnetic field generated by a current applied to the coils.

The main objectives for 2022 will be the finalization of the systematic effect studies and the extraction of the final SME results. The start of the disassembly of the hydrogen beamline is foreseen for the first quarter of 2022. At that time, the cavity assembly will be brought to the AD to perform measurements of the residual magnetic field inside the cavity in the conditions of $\overline{\text{H}}$ data taking (with CUSP and other magnets energized). This will serve as input for the design of compensation coils. This task is of critical importance (compare section 11.1.1) for performing the most precise $\overline{\text{H}}$ ground-state hyperfine splitting measurement.

11.2 Progress at hydrogen deexcitation experiment

This experimental activity follows up on our previous theoretical studies [132] to stimulate the decay of highly excited $\overline{\text{H}}$ states formed at the production point inside the cusp trap. Low number of antihydrogen atoms at the detector (in part due to their high quantum states at production hindering efficient formation of a beam) and long radiative lifetimes of the initially produced states currently inhibit in-beam ground-state hyperfine spectroscopy. In order to mitigate this issue, a first proof-of-principle setup was used to investigate the potential of different light sources for stimulating the deexcitation of high-lying Rydberg states. This work, published in 2021, successfully demonstrated stimulated THz transitions between Rydberg states in cesium atoms using photomixers [133]. Building upon this, work on hydrogen was initiated at CERN in 2020 in view of demonstrating fast stimulated deexcitation to ground-state before implementation to the $\overline{\text{H}}$ setup. Following different hydrogen source characterization measurements carried out in 2020, the exper-

imental activity focused, in the first half of 2021, on building a new hydrogen beamline and a laser room in building 275 to host the beamline and the laser necessary to produce a Rydberg hydrogen beam from a source of ground-state hydrogen. The laser room was expected to be finalized in the first months of 2021, but delays related to new safety requirements with respect to air recycling (the addition of a double-flux chamber was found necessary) and delivery of laser interlocks led to a first availability of the laser room in June 2021. The new hydrogen beamline, pictured in Fig. 42, was installed and commissioned in the summer 2021. It consists of an ultra-pure molecular hydrogen supply line providing a constant flow into a cylindrical 13 mm diameter quartz tube enclosed in an Evenson cavity driving a dissociation plasma. Thermal hydrogen atoms emerge from the plasma region and are emitted into the downstream vacuum region via a circular aperture, mounted into a KF-sealing ring. A first KF160 chamber hosts a two-stage aluminum thermal beam shield which is cooled by compressed helium down to temperatures of 25 K. The shielding prevents thermal radiation from acting upon the quantum state distribution within the beam. Laser access to excite the atomic beam is provided via a quartz viewport and openings in the cryogenic beam shield. The laser beam is guided through the chamber, perpendicular to the atomic beam direction, toward a second viewport where the light can be dumped outside to minimize parasitic heating of the cryogenic beam shield. A second CF160 chamber (operated at pressures $\sim 1 \times 10^{-6}$ mbar) is mounted further down the atoms' flight path where a set of electric field ionizer meshes and two micro-channel plate (MCP) chevron stacks are installed parallel to the beam propagation direction. Ionization products are detected as a function of the electric field ionization strength in view of probing the quantum state distribution within the beam [134]. The DAQ was based on a NI USB-6009 DAQ card operated via LabView allowing to record the count rate of ionization products. It was subsequently upgraded to a digitizer (CAEN DT5720 4-Channel 12bit - 250MS/s) to detect the pulse shape and time-of-flight for each registered event. Access for radiation for Rydberg state mixing, deexcitation and/or beam velocity Doppler measurements is provided through a viewport located at the downstream end of the beamline.
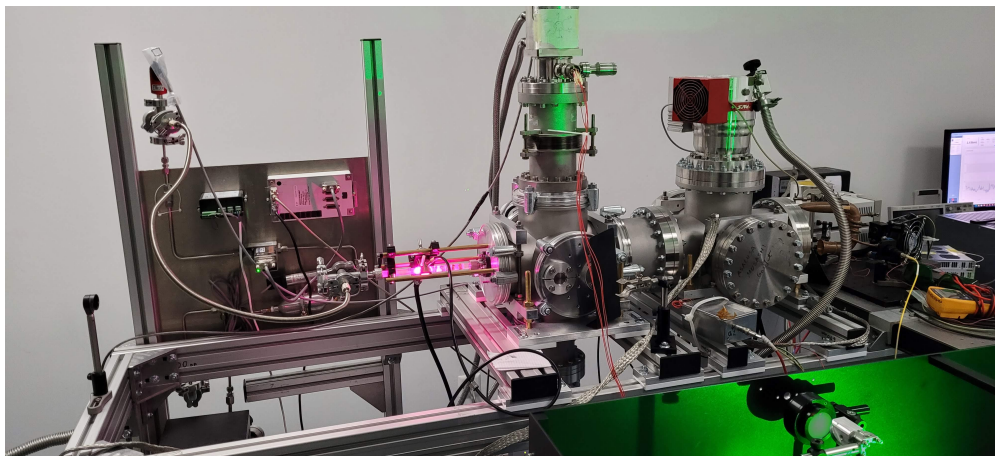
Figure 42 – Photograph of the hydrogen deexcitation setup. Molecular hydrogen is dissociated within a microwave discharge plasma (pink glow). The quantum state distribution of the emitted atomic beam is probed in the most downstream chamber using a tunable electric field. The ionization products are detected with microchannel plate detectors. Access for the Rydberg excitation laser light is provided in the first vacuum chamber.

The Ti:Sa laser for hydrogen excitation to Rydberg states from the 2s state was delivered at the beginning of the summer 2021. In short, it consists of a commercial 10 ns pulsed Nd:YAG

laser (Nano T 290-10 from Litron) which is frequency doubled to 523 nm and fed into a gain switched injection seeded Ti:Sa cavity. The cavity output is frequency doubled with a BBO crystal to obtain light pulses around 364 nm. The design of the laser is based upon a setup discussed in [135]. The laser was provided by collaborators at Laboratoire Aimé Cotton. It was commissioned at CERN in the second half of 2021 and shown to provide some 10 mJ average pulse energies (pulse duration 10 ns) at 364 nm when seeded with a continuous-wave Sacher TEC520 diode laser. Improvements, in particular to the stability of the power output, are currently being pursued, but can be done in parallel to first deexcitation attempts on Rydberg atoms obtained by laser-excitation from the 2s state or directly out of the dissociation source. In this latter case, the broad range of Rydberg states populated reproduces conditions similar to those of the $\overline{\mathrm{H}}$ experiments. The presence of Rydberg hydrogen, observed in 2020 with a different source and a shorter apparatus, was also confirmed in 2021 at the end of the new hydrogen beamline. However, the rate remains low and could not be increased by varying plasma parameters. We note that measurements of Rydberg state distributions are relevant to the plasma community in particular for benchmarking Rydberg formation cross-sections in collisional radiative models such as, for example, Yacora [136] (a publication is being drafted on the measurements taken at different plasma conditions). Despite low rates, first deexcitation attempts on the Rydberg beam from the plasma source, will be done in 2022 using a lamp providing broadband THz radiation. In parallel, work on 2s excitation by electron collision using an apparatus readily developed in 2020 (and detailed in the previous report) will be carried forward to then employ the 2s to 30p excitation laser discussed above. Circular excited states can be obtained via crossed electric and magnetic field method as discussed in [137]. Simulations have been realized by a bachelor student [138] to evaluate the appropriate field configurations and the design of a cross-field region are being pursued at the time of writing. Once the excitation to circular Rydberg states has been demonstrated, fast deexcitation on particular transitions can be attempted. To this purpose, developments of dedicated photomixers have been initiated in collaboration with a french CNRS laboratory. Given the fast developments in powerful THz technologies, deexcitation could possibly be attempted using THz radiation only (instead of a combination of THz light and a powerful deexcitation laser).

We envision first deexcitation results on hydrogen before the end of 2022. Implementation in the ASACUSA $\overline{\overline{\mathrm{H}}}$ setup of the deexcitation apparatus will be studied in details in the coming months.

References

[1] V. I. Korobov, L. Hilico, and J.-P. Karr, *Phys. Rev. Lett.*, vol. 112, p. 103003, 2014.

[2] V. I. Korobov, L. Hilico, and J. -P. Karr, *Phys. Rev. A*, vol. 89, p. 032511, 2014.

[3] V. I. Korobov, *Phys. Rev. A*, vol. 89, p. 014501, 2014.

[4] V. I. Korobov, L. Hilico, and J.-P. Karr, *Hyperfine Int.*, vol. 233, p. 75, 2015.

[5] K. Sakimoto, *Phys. Rev. A*, vol. 91, p. 042502, 2015.

[6] V. I. Korobov, A. K. Bekbaev, D. T. Aznabayev, and S. A. Zhaugasheva, *J. Phys. B*, vol. 48, p. 245006, 2015.

[7] M.-H. Hu *et al.*, *Chem. Phys. Lett.*, vol. 654, p. 114, 2016.

[8] F. Ficek *et al.*, *Phys. Rev. Lett.*, vol. 120, p. 183002, 2018.

[9] D. Baye, J. Dohet-Eraly, and P. Schoofs, *Phys. Rev. A*, vol. 99, p. 022508, 2019.

[10] T. P. Grozdanov and E. A. Solov'ev, *Eur. Phys. J. D*, vol. 74, no. 3, p. 50, 2020.

[11] Z.-D. Bai, Z.-X. Zhong, Z.-C. Yan, and T.-Y. Shi, *Chin. Phys. B*, 2021.

[12] A. Bibikov, G. Y. Korenman, and S. Yudin, *Moscow University Physics Bulletin*, vol. 75, no. 3, p. 213, 2020.

[13] G. Ya. Korenman and S. N. Yudin, *Eur. Phys. J. D*, vol. 75, no. 2, pp. 1–7, 2021.

[14] H. Yamaguchi *et al.*, *Phys. Rev. A*, vol. 66, p. 022504, 2002.

[15] M. Hori *et al.*, *Phys. Rev. Lett.*, vol. 96, p. 243401, 2006.

[16] T. Pask *et al.*, *J. Phys. B*, vol. 41, p. 081008, 2008.

[17] M. Hori *et al.*, *Nature*, vol. 475, p. 484, 2011.

[18] S. Friedreich *et al.*, *J. Phys. B*, vol. 46, p. 125003, 2013.

[19] T. Kobayashi *et al.*, *J. Phys. B*, vol. 46, p. 245004, 2013.

[20] M. Hori *et al.*, *Science*, vol. 354, p. 610, 2016.

[21] M. Hori, H. Aghai-Khozani, A. Sótér, A. Dax, and D. Barna, *Nature*, vol. 581, p. 37, 2020.

[22] A. Sótér *et al.*, *to be published*, 2022.

[23] A. Adamczak and D. Bakalov, *Phys. Rev. A*, vol. 88, p. 042505, 2013.

[24] A. Adamczak and D. Bakalov, *Phys. Rev. A*, vol. 90, p. 054501, 2014.

[25] M. Hori and V. I. Korobov, *Phys. Rev. A*, vol. 81, p. 062508, 2010.

[26] V. Chohan *et al.*, "Extra Low ENergy Antiproton ring (ELENA) and its transfer lines, design report," CERN-2014-002 (CERN, Geneva), 2014.

[27] D. Gamba *et al.*, "ELENA commissioning," in *Proceedings of North American Particle Accelerator Conference NAPAC2019, Lansing MI, USA*, 2019, p. WEYBB1.

[28] A. M. Lombardi, W. Pirkl, and Y. Bylinsky, in *Proceedings of the 2001 Particle Accelerator Conference, Chicago, 2001*. Piscataway, NJ: IEEE, 2001, p. 585.

[29] M. Hori *et al.*, *Phys. Rev. Lett.*, vol. 91, p. 123401, 2003.

[30] S. Alighanbari, G. S. Giri, F. L. Constantin, V. I. Korobov, and S. Schiller, *Nature*, vol. 581, p. 152, 2020.

[31] S. Patra *et al.*, *Science*, vol. 369, no. 6508, p. 1238, 2020.

[32] V. I. Korobov, J.-P. Karr, M. Haidar, and Z.-X. Zhong, *Phys. Rev. A*, vol. 102, no. 2, p. 022804, 2020.

[33] V. I. Korobov and J.-P. Karr, *Phys. Rev. A*, vol. 104, no. 3, p. 032806, 2021.

[34] S. Sturm *et al.*, *Nature*, vol. 506, p. 467, 2014.

[35] F. Heiße *et al.*, *Phys. Rev. Lett.*, vol. 119, p. 033001, 2017.

[36] S. Rau *et al.*, *Nature*, vol. 585, p. 43, 2020.

[37] D. J. Fink and E. G. Myers, *Phys. Rev. Lett.*, vol. 124, no. 1, p. 013001, 2020.

[38] R. Pohl *et al.*, *Science*, vol. 353, no. 6300, p. 669, 2016.

[39] H. Fleurbaey *et al.*, *Phys. Rev. Lett.*, vol. 120, p. 183001, 2018.

[40] W. Xiong *et al.*, *Nature*, vol. 575, p. 147, 2019.

[41] N. Bezginov *et al.*, *Science*, vol. 365, no. 6457, p. 1007, 2019.

[42] A. Grinin *et al.*, *Science*, vol. 370, no. 6520, p. 1061, 2020.

[43] J. DiSciacca *et al.*, *Phys. Rev. Lett.*, vol. 110, no. 13, p. 130801, 2013.

[44] S. Ulmer *et al.*, *Nature*, vol. 524, p. 196, 2015.

[45] M. Ahmadi *et al.*, *Nature*, vol. 557, p. 71, 2018.

[46] R. S. Brusa *et al.*, "The AEgIS experiment at CERN: measuring antihydrogen free-fall in earth's gravitational field to test WEP with antimatter," in *J. Phys.: Conference Series*, vol. 791, no. 1. IOP Publishing, 2017, p. 012014.

[47] D. P. van der Werf and GBAR collaboration, "The GBAR experiment," in *International Journal of Modern Physics: Conference Series*, vol. 30. World Scientific, 2014, p. 1460263.

[48] M. Hori and J. Walz, *Prog. Part. Nucl. Phys.*, vol. 72, p. 206, 2013.

[49] E. J. Salumbides, W. Ubachs, and V. I. Korobov, *J. Mol. Spectrosc.*, vol. 300, p. 65, 2014.

[50] J. Murata and S. Tanaka, *Class Quantum Gravity*, vol. 32, p. 033001, 2015.

[51] M. S. Safronova *et al.*, *Rev. Mod. Phys.*, vol. 90, p. 025008, 2018.

[52] A. S. Lemos, G. C. Luna, E. Maciel, and F. Dahia, *Class. Quantum Gravity*, vol. 36, p. 245021, 2019.

[53] J. Ding *et al.*, *Phys. Rev. Lett.*, vol. 124, no. 16, p. 161801, 2020.

[54] H. Banks and M. McCullough, *Phys. Rev. D*, vol. 103, no. 7, p. 075018, 2021.

[55] M. Germann, S. Patra, J.-Ph. Karr, L. Hilico, V. Korobov, E. Salumbides, K. Eikema, W. Ubachs, and J. Koelemeij, *Phys. Rev. Research*, vol. 3, no. 2, p. L022028, 2021.

[56] Y. J. Kim, P.-H. Chu, and I. Savukov, *Phys. Rev. Lett.*, vol. 121, p. 091802, 2018.

[57] P. Fadeev *et al.*, *Phys. Rev. A*, vol. 99, no. 2, p. 022113, 2019.

[58] J.-P. Karr, M. Haidar, L. Hilico, Z.-X. Zhong, and V. I. Korobov, *Phys. Rev. A*, vol. 102, no. 5, p. 052827, 2020.

[59] M. Hori, *Rev. Sci. Instrum.*, vol. 76, p. 113303, 2005.

[60] M. Hori, K. Yamashita, R. S. Hayano, and T. Yamazaki, *Nucl. Instrum. Methods in Phys. Research A*, vol. 496, p. 102, 2003.

[61] Y. Murakami, H. Aghai-Khozani, and M. Hori, *Nucl. Instrum. Meth. A*, vol. 933, p. 75, 2019.

[62] N. Kuroda, H. A. Torii, K. Y. Franzen, Z. Wang, S. Yoneda, M. Inoue, M. Hori, B. Juhász, D. Horváth, H. Higaki, A. Mohri, J. Eades, K. Komaki, and Y. Yamazaki, *Phys. Rev. Lett.*, vol. 94, no. 2, p. 023401, Jan. 2005.

[63] M. Hori, *Nucl. Instrum. Meth. A*, vol. 522, no. 3, p. 420, 2004.

[64] M. Hori *et al.*, *Phys. Rev. Lett.*, vol. 87, p. 093401, 2001.

[65] M. Agnello *et al.*, *Phys. Rev. Lett.*, vol. 74, p. 371, 1995.

[66] A. Bertin *et al.*, *Phys. Rev. A*, vol. 54, no. 6, p. 5441, 1996.

[67] G. Schiwietz, U. Wille, R. D. Muino, P. Fainstein, and P. Grande, *J. Phys. B*, vol. 29, p. 307, 1996.

[68] R. Cabrera-Trujillo, J. R. Sabin, Y. Öhrn, and E. Deumens, *Phys. Rev. A*, vol. 71, no. 1, p. 012901, 2005.

[69] A. Bianconi, M. Corradini, A. Cristiano, M. Leali, E. L. Rizzini, L. Venturelli, N. Zurlo, and R. Donà, *Phys. Rev. A*, vol. 78, p. 022506, 2008.

[70] A. Lühr and A. Saenz, *Phys. Rev. A*, vol. 79, no. 4, p. 042901, 2009.

[71] J. J. Bailey, A. S. Kadyrov, I. B. Abdurakhmanov, D. V. Fursa, and I. Bray, *Phys. Rev. A*, vol. 92, no. 2, p. 022707, 2015.

[72] A. Bianconi *et al.*, *Phys. Lett. B*, vol. 704, p. 461, 2011.

[73] H. Aghai-Khozani *et al.*, *Eur. Phys. J. Plus*, vol. 127, p. 125, 2012.

[74] M. Corradini *et al.*, *Nucl. Instrum. Meth. A*, vol. 711, p. 12, 2013.

[75] A. Sótér *et al.*, *Rev. Sci. Instrum.*, vol. 85, p. 023302, 2014.

[76] K. Todoroki *et al.*, *Nucl. Instrum. Meth. A*, vol. 835, p. 110, 2016.

[77] H. Aghai-Khozani *et al.*, *Nucl. Phys. A*, vol. 970, p. 366, 2018.

[78] H. Aghai-Khozani *et al.*, *Nucl. Phys. A*, vol. 1009, p. 122170, 2021.

[79] K. Nordlund, M. Hori, and D. Sundholm, "Large nuclear scattering effects in antiproton transmission through polymer and metallic foils," *under evaluation*, 2022.

[80] K. Nordlund, *Comput. Mater. Sci.*, vol. 3, no. 4, p. 448, 1995.

[81] K. Nordlund, D. Sundholm, P. Pyykkö, D. M. Zambrano, and F. Djurabekova, *Phys. Rev. A*, vol. 96, no. 4, p. 042717, 2017.

[82] S. Fabbri and W. Bertsche, "Optimization of antiproton capture for antihydrogen creation in the ALPHA experiment," in *8th Int. Beam Instrum. Conf.*, 2019, pp. 637–641, WEPP040.

[83] B. Obreshkov and D. Bakalov, *Phys. Rev. A*, vol. 93, p. 062505, 2016.

[84] M. Hori, A. Sótér, and V. I. Korobov, *Phys. Rev. A*, vol. 89, p. 042515, 2014.

[85] H. Yamaguchi *et al,*, *Phys. Rev. A*, vol. 70, p. 012501, 2004.

[86] M. Hori *et al.*, *Phys. Rev. Lett.*, vol. 89, p. 093401, 2002.

[87] M. Hori *et al.*, *Phys. Rev. A*, vol. 70, p. 012504, 2004.

[88] M. Hori and A. Dax, *Opt. Lett.*, vol. 34, p. 1273, 2009.

[89] J. Hussels, C. Cheng, E. Salumbides, and W. Ubachs, *Opt. Lett.*, vol. 45, no. 21, p. 5909, 2020.

[90] D. Husmann *et al.*, *Opt. Exp.*, vol. 29, p. 24592, 2021.

[91] A. Jallageas *et al.*, *Metrologia*, vol. 55, p. 366, 2018.

[92] N. Kuroda, H. A. Torii, Y. Nagata, M. Shibata, Y. Enomoto, H. Imao, Y. Kanai, M. Hori, H. Saitoh, H. Higaki, A. Mohri, K. Fujii, C. H. Kim, Y. Matsuda, K. Michishio, Y. Nagashima, M. Ohtsuka, K. Tanaka, and Y. Yamazaki, "Development of a monoenergetic ultraslow antiproton beam source for high-precision investigation," *Phys. Rev. ST Accel. Beams*, vol. 15, p. 024702, Feb 2012. [Online]. Available: https://link.aps.org/doi/10.1103/PhysRevSTAB.15.024702

[93] M. Corradini, M. Leali, E. Rizzini, V. Mascagna, M. Prest, E. Vallazza, and L. Venturelli, "Scintillating bar detector for antiproton annihilations measurements," *Hyperfine Interactions*, vol. 233, no. 1-3, pp. 53–58, 2015. [Online]. Available: https://link.springer.com/article/10.1007/s10751-015-1181-5

[94] G. Andresen, M. Ashkezari, M. Baquero-Ruiz, W. Bertsche, P. Bowe, E. Butler, C. Cesar, S. Chapman, M. Charlton, J. Fajans *et al.*, "Evaporative cooling of antiprotons to cryogenic temperatures," *Physical review letters*, vol. 105, no. 1, p. 013003, 2010.

[95] M. Ahmadi, B. Alves, C. Baker, W. Bertsche, E. Butler, A. Capra, C. Carruth, C. Cesar, M. Charlton, S. Cohen *et al.*, "Antihydrogen accumulation for fundamental symmetry tests," *Nature communications*, vol. 8, no. 1, pp. 1–6, 2017.

[96] B. Radics, D. Murtagh, Y. Yamazaki, and F. Robicheaux, "Scaling behavior of the ground-state antihydrogen yield as a function of positron density and temperature from classical-trajectory monte carlo simulations," *Physical Review A*, vol. 90, no. 3, p. 032704, 2014.

[97] B. Kolbinger, C. Amsler, S. A. Cuendis, H. Breuker, A. Capon, G. Costantini, P. Dupré, M. Fleck, A. Gligorova, H. Higaki *et al.*, "Measurement of the principal quantum number distribution in a beam of antihydrogen atoms," *The European Physical Journal D*, vol. 75, no. 3, pp. 1–14, 2021.

[98] C. Amsler, D. Barna, H. Breuker, S. Chesnevskaya, G. Costantini, R. Ferragut, M. Giammarchi, A. Gligorova, H. Higaki, M. Hori, E. D. Hunter, Y. Kanai, V. Kletzl, V. Kraxberger, N. Kuroda, A. Lanz, M. Leali, V. Mäckel, G. Maero, C. Malbrunot, V. Mascagna, Y. Matsuda, S. Migliorati, D. J. Murtagh, Y. Nagata, A. Nanda, L. Nowak, E. Pasino, W. Pirkl, M. Romé, M. C. Simon, M. Tajima, V. Toso, S. Ulmer, U. Uggerhøj, L. Venturelli, A. Weiser, E. Widmann, T. Wolz, Y. Yamazaki, and J. Zmeskal, "Status report of the ASACUSA experiment - progress in 2020 and plans for 2021," CERN, Geneva, Tech. Rep., Jan 2021. [Online]. Available: https://cds.cern.ch/record/2748998

[99] R. G. Greaves and C. M. Surko, "Inward transport and compression of a positron plasma by a rotating electric field," *Physical Review Letters*, vol. 85, no. 9, pp. 1883–1886, 2000. [Online]. Available: http://link.aps.org/doi/10.1103/PhysRevLett.85.1883

[100] Y. Enomoto, N. Kuroda, K. Michishio, C. H. Kim, H. Higaki, Y. Nagata, Y. Kanai, H. A. Torii, M. Corradini, M. Leali, E. Lodi-Rizzini, V. Mascagna, L. Venturelli, N. Zurlo, K. Fujii, M. Ohtsuka, K. Tanaka, H. Imao, Y. Nagashima, Y. Matsuda, B. Juhász, A. Mohri, and Y. Yamazaki, "Synthesis of cold antihydrogen in a cusp trap," *Phys. Rev. Lett.*, vol. 105, no. 24, p. 243401, Dec 2010.

[101] F. Caspers, private communication, Oct. 2021.

[102] E. D. Hunter, "Minimizing plasma temperature for antimatter mixing experiments," *arXiv:2201.01256*, 2022.

[103] M. Hori and E. Widmann, "ASACUSA status report - recent progress and plans for 2020," CERN, Geneva, Tech. Rep., Jan 2020. [Online]. Available: http://cds.cern.ch/record/2706194

[104] C. Sauerzopf, "The ASACUSA Antihydrogen Detector: Development and Data Analysis," PhD Thesis, Technical University of Vienna, 2016.

[105] M. Fleck, "The Development and Implementation of a Fibre Detector and Advanced Data Acquisition for the ASACUSA Antihydrogen Detector," Master Thesis, Technical University of Vienna, 2018.

[106] PSI and TRIUMF, "MIDAS Wiki." [Online]. Available: https://midas.triumf.ca/MidasWiki/index.php?title=Main_Page&oldid=2982

[107] CAEN S.p.A., "V2495 Programmable Logic Unit PLUS." [Online]. Available: https://www.caen.it/products/v2495/

[108] C. Sauerzopf, "waveformlibrary v1.0.0," 2015.

[109] C. Sauerzopf, L. Gruber, K. Suzuki, J. Zmeskal, and E. Widmann, "Intelligent Front-end Electronics for Silicon photodetectors (IFES)," *Nuclear Instruments and Methods in Physics Research Section A: Accelerators, Spectrometers, Detectors and Associated Equipment*, vol. 819, pp. 163–166, may 2016. [Online]. Available: http://creativecommons.org/licenses/by/4.0/https://linkinghub.elsevier.com/retrieve/pii/S0168900216300158

[110] S. Aghion, O. Ahlén, A. S. Belov, G. Bonomi, P. Bräunig, J. Bremer, R. S. Brusa, G. Burghart, L. Cabaret, M. Caccia, C. Canali, R. Caravita, F. Castelli, G. Cerchiari, S. Cialdi, D. Comparat, G. Consolati, J. H. Derking, S. D. Domizio, L. D. Noto, M. Doser, A. Dudarev, R. Ferragut, A. Fontana, P. Genova, M. Giammarchi, A. Gligorova, S. N. Gninenko, S. Haider, J. Harasimowicz, T. Huse, E. Jordan, L. V. JØrgensen, T. Kaltenbacher, A. Kellerbauer, A. Knecht, D. Krasnický, V. Lagomarsino, A. Magnani, S. Mariazzi, V. A. Matveev, F. Moia, G. Nebbia, P. Nédélec, N. Pacifico, V. Petráček, F. Prelz, M. Prevedelli, C. Regenfus, C. Riccardi, O. RØhne, A. Rotondi, H. Sandaker, A. Sosa, M. A. S. Vasquez, M. Špaček, G. Testera, C. P. Welsch, and S. Zavatarelli, "Detection of low energy antiproton annihilations in a segmented silicon detector," *Journal of Instrumentation*, vol. 9, no. 06, p. P06020, jun 2014. [Online]. Available: https://doi.org/10.1088%2F1748-0221%2F9%2F06%2Fp06020

[111] S. Aghion, O. Ahlén, C. Amsler, A. Ariga, T. Ariga, A. S. Belov, G. Bonomi, P. Bräunig, J. Bremer, R. S. Brusa, L. Cabaret, C. Canali, R. Caravita, F. Castelli, G. Cerchiari, S. Cialdi, D. Comparat, G. Consolati, J. H. Derking, S. D. Domizio, L. D. Noto, M. Doser, A. Dudarev, A. Ereditato, R. Ferragut, A. Fontana, P. Genova, M. Giammarchi, A. Gligorova, S. N. Gninenko, S. Haider, J. Harasimovicz, S. D. Hogan, T. Huse, E. Jordan, L. V. Jørgensen, T. Kaltenbacher, J. Kawada, A. Kellerbauer, M. Kimura, A. Knecht, D. Krasnický, V. Lagomarsino, A. Magnani, S. Mariazzi, V. A. Matveev, F. Moia, G. Nebbia, P. Nédélec, M. K. Oberthaler, N. Pacifico, V. Petráček, C. Pistillo, F. Prelz, M. Prevedelli, C. Regenfus, C. Riccardi, O. Røhne, A. Rotondi, H. Sandaker, P. Scampoli, A. Sosa, J. Storey, M. A. S. Vasquez, M. Špaček, G. Testera, D. Trezzi, R. Vaccarone, C. P. Welsch, and S. Zavatarelli, "Prospects for measuring the gravitational free-fall of antihydrogen with emulsion detectors," *Journal of Instrumentation*, vol. 8, no. 08, p. P08013, aug 2013. [Online]. Available: https://doi.org/10.1088%2F1748-0221%2F8%2F08%2Fp08013

[112] S. Aghion, C. Amsler, M. Antonello, A. Belov, G. Bonomi, R. Brusa, M. Caccia, A. Camper, R. Caravita, F. Castelli, G. Cerchiari, D. Comparat, G. Consolati, A. Demetrio, L. D. Noto, M. Doser, C. Evans, M. Fanì, R. Ferragut, J. Fesel, A. Fontana, S. Gerber, M. Giammarchi, A. Gligorova, F. Guatieri, P. Hackstock, S. Haider, A. Hinterberger, H. Holmestad, A. Kellerbauer, O. Khalidova, D. Krasnický, V. Lagomarsino, P. Lansonneur, P. Lebrun, C. Malbrunot, S. Mariazzi, J. Marton, V. Matveev, S. Müller, G. Nebbia, P. Nedelec, M. Oberthaler, N. Pacifico, D. Pagano, L. Penasa, V. Petracek, F. Prelz, M. Prevedelli, B. Rienaecker, J. Robert, O. RØhne, A. Rotondi, H. Sandaker, R. Santoro, L. Smestad, F. Sorrentino, G. Testera, I. C. Tietje, E. Widmann, P. Yzombard, C. Zimmer, J. Zmeskal, and N. Zurlo, "Antiproton tagging and vertex fitting in a timepix3 detector," *Journal of Instrumentation*, vol. 13, no. 06, pp. P06 004–P06 004, jun 2018. [Online]. Available: https://doi.org/10.1088/1748-0221/13/06/P06004

[113] E. Widmann and M. Hori, "ASACUSA STATUS REPORT Recent progress and plans for LS2," CERN, Geneva, Tech. Rep. CERN-SPSC-2019-006. SPSC-SR-245, Jan 2019. [Online]. Available: https://cds.cern.ch/record/2654222

[114] P. V. Degtyarenko, M. V. Kossov, and H.-P. Wellisch, "Chiral invariant phase space event generator," *The European Physical Journal A*, vol. 8, no. 2, pp. 217–222, Jul 2000. [Online]. Available: https://doi.org/10.1007/s100500070108

[115] A. Galoyan, A. Ribon, and V. Uzhinsky, "Dynamics of Anti-Proton–Protons and Anti-Proton–Nucleus Reactions," *Nucl. Theor.*, vol. 35, pp. 194–202, 2016.

[116] T. Böhlen, F. Cerutti, M. Chin, A. Fassò, A. Ferrari, P. Ortega, A. Mairani, P. Sala, G. Smirnov, and V. Vlachoudis, "The fluka code: Developments and challenges for high energy and medical applications," *Nuclear Data Sheets*, vol. 120, pp. 211 – 214, 2014. [Online]. Available: https://doi.org/10.1016/j.nds.2014.07.049

[117] T. Poikela, J. Plosila, T. Westerlund, M. Campbell, M. D. Gaspari, X. Llopart, V. Gromov, R. Kluit, M. van Beuzekom, F. Zappon, V. Zivkovic, C. Brezina, K. Desch, Y. Fu, and A. Kruth, "Timepix3: a 65k channel hybrid pixel readout chip with simultaneous ToA/ToT and sparse readout," *Journal of Instrumentation*, vol. 9, no. 05, p. C05013, 2014. [Online]. Available: https://doi.org/10.1088/1748-0221/9/05/C05013

[118] C. Amole, G. Andresen, M. Ashkezari, M. Baquero-Ruiz, W. Bertsche, P. Bowe, E. Butler, A. Capra, P. Carpenter, C. Cesar, S. Chapman, M. Charlton, A. Deller, S. Eriksson, J. Escallier, J. Fajans, T. Friesen, M. Fujiwara, D. Gill, A. Gutierrez, J. Hangst, W. Hardy, R. Hayano, M. Hayden, A. Humphries, J. Hurt, R. Hydomako, C. Isaac, M. Jenkins, S. Jonsell, L. Jørgensen, S. Kerrigan, L. Kurchaninov, N. Madsen, A. Marone, J. McKenna, S. Menary, P. Nolan, K. Olchanski, A. Olin, B. Parker, A. Povilus, P. Pusa, F. Robicheaux, E. Sarid, D. Seddon, S. S. E. Nasr], D. Silveira, C. So, J. Storey, R. Thompson, J. Thornhill, D. Wells, D. [van der Werf], J. Wurtele, and Y. Yamazaki, "The alpha antihydrogen trapping apparatus," *Nucl. Instrum. Meth. At*, vol. 735, pp. 319 – 340, 2014. [Online]. Available: https://doi.org/10.1016/j.nima.2013.09.043

[119] N. Kuroda, S. Ulmer, D. J. Murtagh, S. Van Gorp, Y. Nagata, M. Diermaier, S. Federmann, M. Leali, C. Malbrunot, V. Mascagna, O. Massiczek, K. Michishio, T. Mizutani, A. Mohri, H. Nagahama, M. Ohtsuka, B. Radics, S. Sakurai, C. Sauerzopf, K. Suzuki, M. Tajima, H. A. Torii, L. Venturelli, B. Wünschek, J. Zmeskal, N. Zurlo, H. Higaki, Y. Kanai, E. Lodi Rizzini, Y. Nagashima, Y. Matsuda, E. Widmann, and Y. Yamazaki, "A source of antihydrogen for in-flight hyperfine spectroscopy," *Nat Commun*, vol. 5, p. 3089, 01 2014. [Online]. Available: http://dx.doi.org/10.1038/ncomms4089

[120] A. Kellerbauer, Y. Allkofer, C. Amsler, A. S. Belov, G. Bonomi, P. Bräunig, J. Bremer, R. S. Brusa, G. Burghart, L. Cabaret, C. Canali, F. Castelli, K. Chlouba, S. Cialdi, D. Comparat, G. Consolati, L. Dassa, L. Di Noto, A. Donzella, M. Doser, A. Dudarev, T. Eisel, R. Ferragut, G. Ferrari, A. Fontana, P. Genova, M. Giammarchi, A. Gligorova, S. N. Gninenko, S. Haider, J. P. Hansen, F. Haug, S. D. Hogan, L. V. Jørgensen, T. Kaltenbacher, D. Krasnický, V. Lagomarsino, S. Mariazzi, V. A. Matveev, F. Merkt, F. Moia, G. Nebbia, P. Nédélec, T. Niinikoski, M. K. Oberthaler, D. Perini, V. Petráček, F. Prelz, M. Prevedelli, C. Regenfus, C. Riccardi, J. Rochet, O. Røhne, A. Rotondi, M. Sacerdoti, H. Sandaker, M. Špaček, J. Storey, G. Testera, A. Tokareva, D. Trezzi,

R. Vaccarone, F. Villa, U. Warring, S. Zavatarelli, A. Zenoni, and T. A. Collaboration, "The aegis experiment at cern," *Hyperfine Interactions*, vol. 209, no. 1, pp. 43–49, 2012. [Online]. Available: https://doi.org/10.1007/s10751-012-0583-x

[121] P. Pérez, D. Banerjee, F. Biraben, D. Brook-Roberge, M. Charlton, P. Cladé, P. Comini, P. Crivelli, O. Dalkarov, P. Debu, A. Douillet, G. Dufour, P. Dupré, S. Eriksson, P. Froelich, P. Grandemange, S. Guellati, R. Guérout, J. M. Heinrich, P.-A. Hervieux, L. Hilico, A. Husson, P. Indelicato, S. Jonsell, J.-P. Karr, K. Khabarova, N. Kolachevsky, N. Kuroda, A. Lambrecht, A. M. M. Leite, L. Liszkay, D. Lunney, N. Madsen, G. Manfredi, B. Mansoulié, Y. Matsuda, A. Mohri, T. Mortensen, Y. Nagashima, V. Nesvizhevsky, F. Nez, C. Regenfus, J.-M. Rey, J.-M. Reymond, S. Reynaud, A. Rubbia, Y. Sacquin, F. Schmidt-Kaler, N. Sillitoe, M. Staszczak, C. I. Szabo-Foster, H. Torii, B. Vallage, M. Valdes, D. P. Van der Werf, A. Voronin, J. Walz, S. Wolf, S. Wronka, and Y. Yamazaki, "The gbar antimatter gravity experiment," *Hyperfine Interactions*, vol. 233, no. 1, pp. 21–27, Aug 2015. [Online]. Available: https://doi.org/10.1007/s10751-015-1154-8

[122] W. A. Bertsche, "Prospects for comparison of matter and antimatter gravitation with alpha-g," *Phil. Trans. R. Soc. A.*, vol. 376, no. 20170265, 2018. [Online]. Available: http://doi.org/10.1098/rsta.2017.0265

[123] H. S. Plendl, H. Daniel, T. von Egidy, T. Haninger, F. S. Hartmann, P. Hofmann, Y. S. Kim, H. Machner, G. Riepe, J. Jastrzebski, A. Grabowska, W. Kurcewicz, P. Lubinski, A. Stolarz, A. S. Botvina, Y. S. Golubeva, A. S. Iljinov, V. G. Nedorezov, A. S. Sudov, and K. Ziock, "Antiproton-nucleus annihilation at rest," *Physica Scripta*, vol. 48, no. 2, pp. 160–163, aug 1993.

[124] C. Amsler *et al.*, "ASACUSA proposal for ELENA," CERN-SPSC-2019-035 / SPSC-P-307-ADD-2. [Online]. Available: https://cds.cern.ch/record/2691506

[125] A. Boudard, J. Cugnon, J.-C. David, S. Leray, and D. Mancusi, "New potentialities of the Liège intranuclear cascade model for reactions induced by nucleons and light charged particles," *Phys. Rev. C*, vol. 87, p. 014606, Jan 2013. [Online]. Available: https://link.aps.org/doi/10.1103/PhysRevC.87.014606

[126] P. R. Mahaffy and K. Lai, "An electrostatic quadrupole deflector for mass spectrometer applications," *Journal of Vacuum Science & Technology A*, vol. 8, no. 4, pp. 3244–3246, 1990. [Online]. Available: https://doi.org/10.1116/1.576571

[127] D. Manura and D. Dahl, "SIMION (R) 8.1 User Manual (Scientific Instrument Services, Inc. Ringoes, NJ 08551." [Online]. Available: http://simion.com/,2008)

[128] C. Malbrunot, M. Diermaier, M. Simon, C. Amsler, S. A. Cuendis, H. Breuker, C. Evans, M. Fleck, B. Kolbinger, A. Lanz, M. Leali, V. Maeckel, V. Mascagna, O. Massiczek, Y. Matsuda, Y. Nagata, C. Sauerzopf, L. Venturelli, E. Widmann, M. Wiesinger, Y. Yamazaki, and J. Zmeskal, "A hydrogen beam to characterize the asacusa antihydrogen hyperfine spectrometer," *Nuclear Instruments and Methods in Physics Research Section A: Accelerators, Spectrometers, Detectors and Associated Equipment*, vol. 935, pp. 110 – 120, 2019. [Online]. Available: http://www.sciencedirect.com/science/article/pii/S0168900219305315

[129] M. C. Simon, *Rabi Experiments on the σ and π Hyperfine Transitions in Hydrogen and Status of ASACUSA's Antihydrogen Program*, pp. 1–4. [Online]. Available: https://www.worldscientific.com/doi/abs/10.1142/9789811213984_0001

[130] M. Diermaier, C. B. Jepsen, B. Kolbinger, C. Malbrunot, O. Massiczek, C. Sauerzopf, M. C. Simon, J. Zmeskal, and E. Widmann, "In-beam measurement of the hydrogen hyperfine splitting and prospects for antihydrogen spectroscopy," *Nat Commun*, vol. 8, Jun. 2017.

[131] M. Ahmadi, B. X. R. Alves, C. J. Baker, W. Bertsche, E. Butler, A. Capra, C. Carruth, C. L. Cesar, M. Charlton, S. Cohen, R. Collister, S. Eriksson, A. Evans, N. Evetts, J. Fajans, T. Friesen, M. C. Fujiwara, D. R. Gill, A. Gutierrez, J. S. Hangst, W. N. Hardy, M. E. Hayden, C. A. Isaac, A. Ishida, M. A. Johnson, S. A. Jones, S. Jonsell, L. Kurchaninov, N. Madsen, M. Mathers, D. Maxwell, J. T. K. McKenna, S. Menary, J. M. Michan, T. Momose, J. J. Munich, P. Nolan, K. Olchanski, A. Olin, P. Pusa, C. O. Rasmussen, F. Robicheaux, R. L. Sacramento, M. Sameed, E. Sarid, D. M. Silveira, S. Stracka, G. Stutter, C. So, T. D. Tharp, J. E. Thompson, R. I. Thompson, D. P. van der Werf, and J. S. Wurtele, "Observation of the hyperfine spectrum of antihydrogen," *Nature*, vol. 548, p. 66, aug 2017. [Online]. Available: http://dx.doi.org/10.1038/nature23446

[132] T. Wolz, C. Malbrunot, M. Vieille-Grosjean, and D. Comparat, "Stimulated decay and formation of antihydrogen atoms," *Phys. Rev. A*, vol. 101, p. 043412, Apr 2020. [Online]. Available: https://link.aps.org/doi/10.1103/PhysRevA.101.043412

[133] M. Vieille-Grosjean, E. Dimova, Z. Mazzotta, D. Comparat, T. Wolz, and C. L. S. Malbrunot, "Induced THz transitions in Rydberg caesium atoms for application in antihydrogen experiments," *The European Physical Journal D*, vol. 75, no. 1, p. 27, 2021.

[134] T. Wolz, "Controlled manipulation of atoms in rydberg quantum states for application in experiments with antihydrogen," Ph.D. dissertation, Technische Universität, Darmstadt, 2022, in press.

[135] P. Lottigier, A. Jucha, L. Cabaret, C. Blondel *et al.*, "Single-mode scannable nanosecond Ti:sapphire laser for high-resolution two-photon absorption laser-induced fluorescence (TALIF)," *Appl. Phys. B*, vol. 125, no. 14, 2019.

[136] D. Wünderlich, M. Giacomin, R. Ritz, and U. Fantz, "Yacora on the Web: Online collisional radiative models for plasmas containing H, H2 or He," *J. Quant. Spectrosc. Radiat.*, vol. 240, p. 106695, 2020.

[137] R. Lutwak, J. Holley, P. P. Chang, S. Paine *et al.*, "Circular states of atomic hydrogen," *Phys. Rev. A*, vol. 56, pp. 1443–1452, 1997.

[138] P. Kulkarni, "Rydberg excitation of hydrogen for studies towards antihydrogen deexcitation," Bachelor Thesis, Universität Leipzig, 2019.